" THE EFFECTS OF PROPERTIES, MICROSTRUCTURE AND PHASE TRANSFORMATION ON THE EROSION OF HARD MATERIALS"

RICHARD ALAN DOYLE

A dissertation submitted in fulfilment of the requirements for the degree of Master of Science in Applied Science.

University of Cape Town

1989

SYNOPSIS

A variety of ceramic and ultrahard materials have been subjected to both solid particle and cavitation erosion. The materials tested include three grain sizes of alumina, stabilised zirconias, sialon, cubic boron nitride and polycrystalline diamond, and these have a range of microstructural, physical and mechanical properties. The damage modes are described for the two types of erosion and the results are critically discussed.

It has been shown that different properties and microstructural features control the respective types of erosion. Hardness is the critical property which controls material loss during solid particle erosion. Cavitation erosion in contrast is less sensitive to hardness, but is extremely defect sensitive and preferentially attacks weak or damaged regions on the target. Grain size and shape, and the properties of the grain boundary or intergranular phase exert a strong influence on both types of erosion. It has in addition been concluded that a propensity for a stress induced phase transformation, such as that exhibited by stabilised zirconia, will benefit the resistance of a ceramic to erosion.

Ultrahard materials generally outperform the structural ceramics that were tested. While it was not possible to ascertain the effects of grain size conclusively, a large extent of intergrowth between the crystallites during manufacture appears to be beneficial to erosion resistance.

ACKNOWLEDGEMENTS

I would like to thank all those who have assisted me in the research work reported in this thesis.

At the outset I wish to thank Professor A. Ball for his supervision and encouragement during the course of this project.

I am also very grateful to Helgard Bohm, Sue Betz, Nick Dreze, Bernie Greeves, Glen Newins, James Petersen, and Reggie Hendricks for their advice and assistance both in the laboratory and in the preparation of this manuscript.

Further, I am thankful for the cooperation and feedback from my fellow students. In particular, I am extremely grateful to Candy Lang for her moral support and intellectual feedback throughout this project and to Dr. M. Shaw for frequent advice and assistance.

Finally, the support of the De Beers Industrial Diamond Division Diamond Research Laboratory is gratefully acknowledged, and the Council for Scientific and Industrial Research are thanked for my FRD bursary. The Diamond Research laboratory and the National Institute of Materials Research at the Council for Scientific and Industrial Research are also thanked for their generous supply of materials.

LIST OF SYMBOLS AND ABBREVIATIONS:

a -	characteristic contact dimension
A -	cross sectional area
A16/17 -	alumina grades 16 and 17
b -	plastic zone radius
B -	width
c -	cubic
C_p -	specific heat
d -	chordal radius of eroded area
e -	elongation
E -	Young's modulus
f_a -	volume fraction of phase (a)
H -	hardness
HCP -	hexagonal close packed
HF -	hydrofluoric acid
I_x(abc) -	integrated intensity of x-ray peak (abc) of phase (x)
k -	thermal conductivity
K -	thermal diffusivity (K=k/qC)
K_c -	fracture toughness
m -	monoclinic
P -	load
P_r -	pressure
PCD -	polycrystalline diamond
PCBN -	polycrystalline cubic boron nitride
PSZ -	partially stabilised zirconia
r_p -	particle radius
R -	alumina grade RCHPDBM
S.P.E. -	solid particle erosion
t -	tetragonal
T -	temperature

TRIP - transformation induced plasticity

TZP - Tetragonal Zirconia Polycrystal

v - particle velocity

x_d - root mean square diffusion distance from impact site

x_i - distance that heat diffuses in the interval between impacts

x_p - depth of plastic zone associated with impact

YAG - yttrium aluminium garnet

ZTA - zirconia toughened alumina

2/3YTZP - Tetragonal Zirconia Polycrystal containing 2 or 3 percent of yttria respectively

ρ - density

ρ_p - particle density

CONTENTS

		Page
SYNOPSIS		(i)
ACKNOWLEDGEMENTS		(ii)
LIST OF SYMBOLS AND ABBREVIATIONS		(iii)
Chapter 1:	INTRODUCTION	1
Chapter 2:	LITERATURE REVIEW	5
2.1	Solid Particle Erosion	5
2.1.1	Single impacts: basic mechanisms	5
2.1.2	Predictive theories of erosion	7
2.1.3	Microstructural Effects	8
2.1.4	Thermal Effects	9
2.1.5	Effect of stress induced Transformation	10
2.2	Cavitation Erosion	12
2.2.1	Previous work	12
2.2.2	Theories of cavitation	12
2.2.3	Prediction of material response	14
2.2.4	Effects of transformation on erosion	15
Chapter 3:	MATERIALS UNDER INVESTIGATION	16
3.1	Ceramic Materials	16
3.1.1	Stabilised zirconias	16
3.1.1.1	Partially stabilised zirconia	17

	3.1.1.2	Tetragonal zirconia polycrystals	19
	3.1.2	Sialon	21
	3.1.3	Alumina	21
	3.2	Ultrahard Materials	22
	3.2.1	Polycrystalline diamond	22
	3.2.2	Polycrystalline cubic boron nitride	23
Chapter 4:	EXPERIMENTAL PROCEDURES		24
	4.1	Preparation	24
	4.2	Characterisation	24
	4.2.1	Porosity	24
	4.2.2	Grain size determination	24
	4.2.3	Mechanical testing	25
	4.2.4	Energy dispersive spectroscopy	25
	4.3	Solid Particle Erosion	26
	4.3.1	Erosion rig	26
	4.3.2	Single impacts and steady state testing	26
	4.3.3	Dislocation substructure	27
	4.4	Cavitation Erosion	27
	4.4.1	Cavitation erosion rig and procedure	27
	4.5	Microscopy	28
	4.5.1	Optical microscopy	28
	4.5.2	Scanning electron microscopy	29
	4.6	X-ray diffraction	29
Chapter 5:	RESULTS		30
	5.1	Characterisation of Materials	30
	5.2	Solid Particle Erosion	31
	5.2.1	Lithium fluoride	31
	5.2.2	Ceramic materials	32
	5.2.3	Ultrahard materials	36

5.2.4 Silicon carbide grit 38
5.2.6 Adiabatic melting during the erosion of alumina 39
5.2.7 Evaluation of erosion resistance 41
5.3 Cavitation Erosion 45
5.3.1 Ceramics 45
5.3.2 Ultrahard materials 49
5.3.3 Cavitation erosion performance 51
5.3.4 X-ray diffraction evaluation of stress induced tetragonal to monoclinic transformation in zirconia 55

Chapter 6: DISCUSSION 58
6.1 Solid Particle Erosion 58
6.1.1 Individual material response 58
6.1.1.1 Ceramic materials 58
6.1.1.1.1. Polycrystalline aluminium oxide 58
6.1.1.1.1.1 Single impacts: basic erosion mechanisms 58
6.1.1.1.1.2 Steady state erosion 60
6.1.1.1.1.3 Thermomechanical effects during erosion of alumina 62
6.1.1.1.2 Sialon 72
6.1.1.1.2.1 Single impacts: basic erosion mechanism 72
6.1.1.1.2.2 Steady state erosion 72
6.1.1.1.3 Zirconia 73
6.1.1.1.3.1 Single impacts: basic erosion mechanisms 73
6.1.1.1.3.2 Steady state erosion 73
6.1.1.1.3.3 The effect of transformation on erosion response 73

6.1.1.2 Superhard materials 74
6.1.1.2.1 Cubic boron nitride 74
6.1.1.2.2 Polycrystalline diamond 75
6.1.2 Comparisons between materials 75
6.2 Cavitation Erosion 77
6.2.1 Individual material responses 77
6.2.1.1 Alumina 77
6.2.1.1.1 Initiation and basic mechanisms of damage 77
6.2.1.1.2 Steady state 78
6.2.1.2 Sialon 78
6.2.1.2.1 Initiation and basic mechanisms 78
6.2.1.2.2 Steady state 79
6.2.1.3 Zirconia 79
6.2.1.3.1 Partially stabilised zirconia 79
6.2.1.3.1.1 Initiation and basic mechanisms 79
6.2.1.3.1.2 Steady state 81
6.2.1.3.2 Tetragonal zirconia polycrystal 81
6.2.1.3.2.1 Initiation and basic mechanisms of damage 81
6.2.1.3.2.2 Steady state 81
6.2.1.2.2.3 Transformation effects 81
6.2.1.4 Cubic boron nitride 83
6.2.1.4.1 Initiation and basic mechanisms 83
6.2.1.4.2 Steady state erosion 83
6.2.1.5 Polycrystalline diamond 83
6.2.1.5.1 Initiation and basic mechanisms 83
6.2.1.5.2 Steady state 84
6.2.1.6 Comparisons between materials 84

Chapter 7: SUMMARY AND CONCLUSIONS 86

REFERENCES 88

CHAPTER 1.

INTRODUCTION

Hard materials are finding ever-increasing application in industry where their resistance to a variety of aggressive environments and their superior performance in demanding applications is found to be beneficial. Wear and failure, which may often be catastrophic, are nevertheless inevitable but may be alleviated either by design or suitable choice of materials. Such a choice is often difficult because of the complexity of tribological problems which frequently involve the combined actions of physical, mechanical, thermal, and sometimes chemical forces.

Considerable work has been undertaken on the resistance of metallic alloys, surface treatments and coatings to erosion, but there is a paucity of published research on the performances of new structural ceramics and ultrahard materials[1,2,3]. Consequently there is still insufficient knowledge of many of the fundamental modes of erosion damage in these materials.

The pragmatic importance of an understanding of solid particle erosion lies in the fact that many industrial processes involve the transport of small hard particles in a fluid stream. Erosive wear occurs here where such streams impinge on components. Common examples are the damage experienced in gas turbines and the tail nozzles of rocket motors[4]. Figure 1 presents a schematic of a typical impact on a ceramic target and the important features are pointed out.

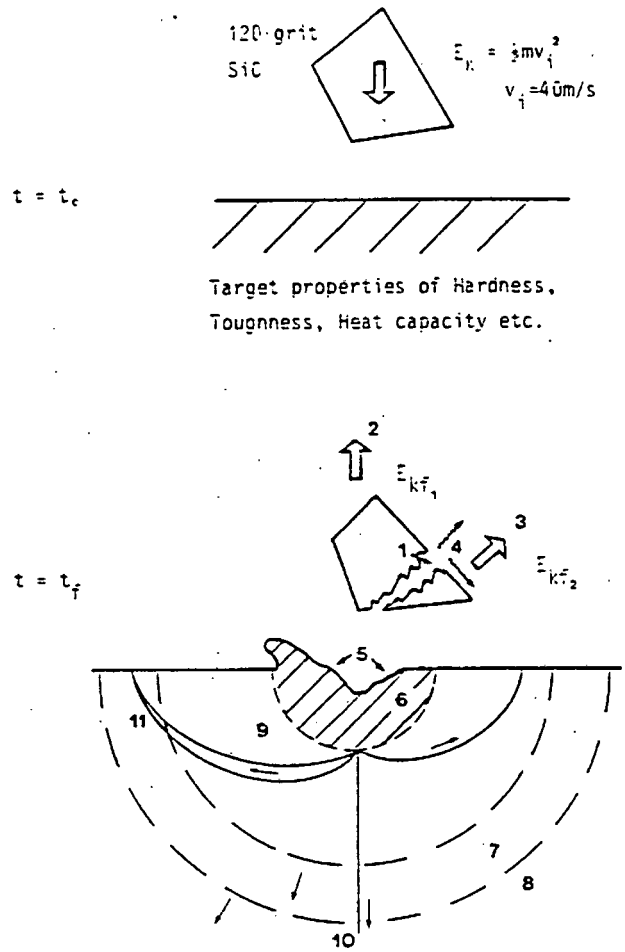

1: Fracture of SiC
2: Fragment recoil momentum
3: "
4: Triboluminescence due to 1
5: Frictional heating at contact
6: Plastic zone- dissipation of energy as heat
7: Shear wave
8: Compressive wave
9: Lateral venting on unloading cycle due to residual elastic-plastic stresses
10: Radial cracking
11: Lateral venting may reach surface and result in spallation

Fig. 1 Schematic representation of impact and subsequent partitioning of energy.

Cavitation erosion on the other hand can occur in almost all hydrodynamic systems and turbomachines including pumps, turbines and hydrofoils[5]. Where a fluid is subjected to cyclic pressure changes, the nucleation and collapse of cavities in that liquid may result in severe damage to materials in contact with the liquid. A schematic of bubble collapse is presented in figure 2.

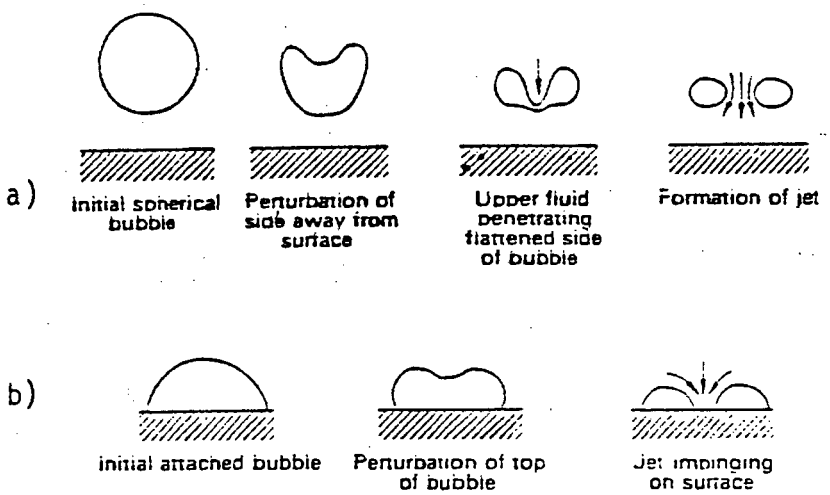

Fig. 2 Collapse of cavity and formation of microjet[3].
a) cavity near surface
b) cavity attached to surface of target.

Solid particle erosion and cavitation erosion are characterised by high strain rates, but subject target materials to stress systems which differ in nature, magnitude and extent. Material response to each type of erosion is thus expected to be different and to be controlled by different properties. Both types of erosion do

however result in unacceptable loss of material and in degradation of strength.

It is the aim of this dissertation then to determine and understand the response of various hard materials to solid particle and cavitation erosion. The influences of external parameters such as erosive particle hardness and internal variables including microstructure are critically discussed. This should help to enable real predictions to be made concerning the optimal conditions and materials for erosion resistance. Further, it is hoped that the investigation of these modern structural hard materials under the extreme conditions of erosion will further the general understanding of various aspects of the deformation and fracture of hard materials.

CHAPTER 2.

LITERATURE REVIEW

2.1. SOLID PARTICLE EROSION.

2.1.1 Single Impacts: Basic mechanisms.

Sheldon and Finnie[6] are generally acknowledged to be the first workers to report the ductile behaviour of nominally brittle materials during erosion[7]. This was attributed to the statistical variation of strength in ceramics which predicts significant size effects. Although there has been fairly extensive research on the erosion of well characterised ceramics since, there has in general been a paucity of work on many of the latest stuctural hard materials under investigation here (Table 1).

It is widely recognised that an elastic-plastic interaction is dominant in the solid particle erosion of ceramics within a critical particle size regime[8]. Compressive hydrostatic stresses below the indentation suppress fracture but do not affect the critical resolved shear stresses which control dislocation plasticity[9]. The size affect arises directly out of the dependence of the fracture toughness on the local flaw distribution. As the interaction area becomes smaller the chance of the elastic deformation boundary including a large flaw decreases and the material's strength tends toward its intrinsic value[10].

Radial and lateral cracking are present in the elastic-plastic regime as well as intense dislocation plasticity below the impact[10,11,12]. The damage process is similar in

character to quasi-static indentation. The cracks propagate on planes perpendicular to the maximum principal tensile stresses; radial cracking is initiated during the loading cycle as an accommodating mechanism[13]. This contributes to strength degradation. Lateral cracks initiate parallel to the surface of the material and curve upward towards the surface of the target during the unloading cycle. These latter cracks are controlled by the residual elastic-plastic mismatch stress field which results from constraint of the plastic zone by the matrix[14]. Intersection of lateral vents with the surface results in spallation of material and consequently material loss.

The relative extent of fracture and plasticity depends on the type of bonding in the target material[15] and the duration and magnitude of the stress field exerted on the target by the impacting particle. Because of the elastic-plastic nature of the phenomenon, it is apparent that both the target material's resistance to flow (hardness: H) and resistance to fracture (fracture toughness: K_c) are important controlling properties. The importance of the use of the appropriate dynamic values of these parameters is emphasised[11]. Experiments investigating the effects of temperature on erosion normal to the target surface indicate that material removal is controlled primarily by toughness[15]. This conclusion was reached since erosion results at room temperature and at 1000 degrees celcius showed little significant difference . While the fracture toughness shows little change over this range, the flow stress changes significantly. Nevertheless the formation and growth of the plastic zone during impact determines the type of cracks formed[10]. More work is required to fully understand and quantify the relationships between plasticity and fracture.

2.1.2: Predictive theories of erosion.

Several attempts have been made to develop theories which predict erosion performance from the relevant target, particle and erosion parameters. In general however, the complexity of the problem has made a rigorous theoretical derivation intractable. The lack of quantitative information on material response at the high strain rates experienced, and incomplete understanding both of the effects of adiabatic heating and the large compressive stresses exerted on the target, have been largely responsible for these difficulties[11]. The result is that most treatments have been semi-empirical dimensional analyses.

These theories are developed from analysis of a single impact and are extended to erosion by assumptions concerning the extent of the interaction between adjacent or concentric impacts (i.e. the efficacy of material removal per impact). Two main approaches have developed which differ in their assumed dependence of impact load (P) on the kinetic and material parameters that are important to erosion[16].

The first is the theory due to Evans[10,17] which includes dynamic stress wave effects in the calculation of P. The other theory has been developed by Wiederhorn and Lawn[18] and is based on the observations of the similarities between quasi-static indentation and particle impact.

Both expressions relate erosion to the depth of damage and area of lateral cracking. In both cases the extent of lateral cracking is determined by the Roesler equation[19]. The major differences are in the erosive dependences on particle density and velocity, and target hardness. The fracture toughness term is clearly dominant. It is important

to note that both theories treat single impacts on isotropic materials in idealised conditions.

Several workers have compared their experimental results with the theories and all have found that both agree qualitatively in the correct impact regime[20,21]. Evans[17], and subsequently Wiederhorn and Hockey[16] and Kingon et al[22], have found that the hardness term underestimates the experimental result. The general agreement of results with both theories may be rationalised in terms of the dominant K_{IC} term. The lack of quantitative agreement is certainly due to the simplifying assumptions in the theoretical derivations. Dimond[21] has suggested that a term should be introduced into the theory which accounts for angularity of the erosive particle. Further the assumption that all impacts result in material removal is patently incorrect and it has been observed that interaction effects do play a role. Thus the assumption by Evans[17] and Wiederhorn and Hockey[16] that impacts are independent is not accurate.

Finally the theory ignores any microstructural effects on erosion and this is thought to be an important reason for the discrepancy with theory[16,22].

2.1.3: Microstructural effects:

The theories of erosion that have been developed assume that ceramics are single phase isotropic materials. In general of course such materials are far more complex in microstructure. Because they are brittle, it is widely accepted that the grain size of the material can be equated with the metastable flaw (precursor) size[23]. In addition to the expected and observed effects of grain size on toughness and hardness, it is expected that anisotropy[16] and porosity[22] will both play a role in erosion performance. Further it has been pointed out that H and K_c must be

evaluated at the appropriate microstructural level[24] so that microstructural interactions, including crack arrests at interfaces, grain boundaries and porosity can be understood.

Rickerby[11] has drawn attention to the fact that in addition to H and K_c being considered at the correct scale, their dynamic values pertain at the high strain rates encountered during erosion. Quasi-static room temperature evaluation of these parameters may therefore yield inappropriate information. There still exists some controversy as to the effect of microstructure. Both Gulden[20] and Wiederhorn and Hockey[16] have considered the effect of microstructure on the discrepancy between the theories of erosion and their results. While Gulden thought that the microstructural variations in her material were adequately accounted for by H and K, Wiederhorn and Hockey attributed the discrepancy directly to microstructural factors. Ritter[25] found that erosion of polycrystalline alumina was not a function of microstructure, but his experiment involved the impact of large (127-1016 micron) particles on the target and the interaction was apparently entirely brittle and consequently out of the elastic-plastic regime.

2.1.4: Thermal effects.

Solid particle erosion is characterised by high strain rates, large strains and localised deformation. Under these conditions, concomitant thermomechanical effects are expected, and there have been extensive reports of the formation of adiabatic shear bands and even melting of metals[26,27]. Melting was first observed during the erosion of ceramics by Yust and Crouse[28]. Although the melting points of ceramics are high, they are good insulators and this favours adiabatic conditions.

Yust and Crouse observed stringer and droplet type features at the exit side of craters formed during the erosion of alumina and mullite. They considered this phenomenon to be analogous to the observations by Hutchings[26] of adiabatic shear bands in the same part of craters of eroded metal. Yust and Crouse applied the theory of Recht[29] who had earlier considered catastrophic thermoplastic shear and calculated that temperatures of the order of the melting temperature of alumina could be reached under their experimental conditions.

Lawn, Hockey and Wiederhorn[30] also observed melting during erosion of soda-lime glass and used simple indentation theory and the assumptions of adiabatic conditions to calculate the maximum temperature that could be reached. Their calculation involved integration of the work dissipated as heat due to plastic deformation as a function of distance below the contact interface. The calculation facilitated the equation of distance with maximum temperature so that one could ascertain how thick a layer of material could be expected to melt if one knew the impact conditions and the melting point of the material.

The precise mechanism of heat generation and the nature and extent of the thermal cycle at an impact site on a ceramic are still not well known however[11]. Neither are the effects of this thermomechanical event on the severity of erosion.

2.1.5: Effect of stress induced transformation.

Technological developement of structural ceramics is demanded by the number of potential uses for their intrinsic hardness. One of the largest problems associated with this hardness is the brittleness of the materials. The development of transformation toughened zirconia has

resulted in the production of ceramics with unprecedented toughnesses. But while it is well established that the stress induced tetragonal (t) to monoclinic (m) transformation has beneficial implications for quasi-static properties, a systematic investigation of the effect of the transformation on dynamic situations has yet to be undertaken[31]. Lange[32] conducted solid particle erosion tests on zirconia toughened alumina (ZTA) and has demonstrated a novel technique for characterisation of brittle damage during erosion of these materials. These results have implications for the calculation of interaction effects. No investigation of the effect of transformation was undertaken.

Giovanola[31] has also conducted erosion on ZTA and showed that the number and extent of radial cracks due to impact decrease with an increase in tetragonal content of the material. They showed that a critical tetragonal content existed to optimise erosion. This is due to competing effects of increasing compressive stresses in the surface of the material and decreasing hardness with increasing tetragonal content. Pennefather, Hankey, Hutchings and Ball [33] have shown that PSZ performs relatively well, but the precise mechanisms of the resistance to erosion have not been evaluated. The same is true for Kingon, Stone and Carr[22] who have evaluated several zirconia based ceramics. They have shown that the equations due to Evans[17] and Wiederhorn and Lawn[18] underestimate the effect of hardness and also note that microstructural features are not adequately accounted for by the H and K as discussed above. There is however no detailed discussion of the interaction between the transformation mechanism and the stress system due to the impact.

2.2: CAVITATION EROSION

2.2.1: Previous work:

Heathcock, Ball and Protheroe[34] and Ball and Paterson[35] have ranked the performances of several ceramic and cermet materials. Emphasis was however largely on the performance of the cermets and the erosion resistance of the ceramics was investigated for comparison. Miyoshi, Hattorii, Okada and Buckley[36] have investigated the effect of cavitation on single crystal and polycrystalline silicon carbide. Their results showed the sensitivity of this type of attack to surface defects, both extrinsic and intrinsic. Little other work seems to have been conducted on hard materials and the theories of cavitation that have been developed have largely been based on data from tests on metals.

2.2.2: Theories of cavitation:

Vibratory cavitation occurs when the pressure in a liquid is reduced at constant temperature to below the vapour pressure by dynamic means. It is a phenomenon that transforms the low energy density of a pressure field in a liquid into the high energy density associated with the neighbourhood and interior of a collapsing cavity[37]. The tensile stresses induced in the fluid then cause cavity formation. The magnitude of these stresses is below the tensile strength of the liquid because of heterogenous nucleation. Rayleigh[38] has analysed the dynamics of bubble growth and shown the relationships that exist between bubble size and pressure in the liquid and bubble.

As the pressure increases again, a bubble stops growing and when the ambient pressure in the cavitation zone increases above the pressure in the cavity, it collapses violently

resulting in a pressure wave[39]. In addition to the recurring impact from these pressure waves, if the cavity is constrained by proximity to a surface, involution occurs and a liquid microjet is formed which impinges on the surface[39]. The pressure wave itself is rapidly attenuated so that only single bubbles near the surface of a material are thought to cause significant damage[40]. Attenuation of the pulse requires the bubble to be less than its maximum radius from the surface of the target[41]. Hansson[42] has proposed that the collapse of clouds of cavities in concert may however result in damage being caused by cavitation at greater distances from the surface of the target.

The Rayleigh analysis[38] shows that when a collapsing bubble reaches 1/20 of its initial maximum radius, a pressure of 130 MPa will be induced in a liquid. Knapp et al[3] have sophisticated the theory to show that pressures between 20 and 400 MPa may be induced while Preece[39] has estimated from considerations of concerted bubble collapse that pressures as great as 1000 MPa are typical. Observations of damage in high strength materials support this estimate.

Hansson[42] has presented arguments which suggest that during high intensity cavitation, the cloud collapse dominates erosion, while at lower intensities, erosion occurs primarily by liquid jet impact.

It is now generally agreed that the mechanism of attack from the cavitation is one of mechanical stressing. The fatigue type accumulation of plastic damage observed in metals[35] is however thought to be insignificant in the hard materials in this study. Miyoshi et al[36] have shown that dislocation arrays are introduced into the {0001} plane of single crystals of silicon carbide, and that the extent of this plastic deformation increases with time of cavitation. The erosion rates of these single crystals were however

significantly lower than the erosion rate of polycrystalline material where other mechanisms were dominant. In this latter case, it was noted that the depth and number of pores increased during cavitation. There is consequently scope for further work on the conditions governing which mechanisms are dominant in various microstructural modifications of polycrystalline ceramics. This provides some justification for the present investigation into the mechanisms of cavitation erosion of such materials.

2.2.3: Prediction of material response.

Several attempts have been made to correlate the structure and microstructure of metallic materials with their responses to attack by cavitation erosion. Although many of the conclusions pertain only within small groups of similar materials and will not extend in a simple manner to ceramics, a brief discussion of the work that has been done is warranted 1) by the general information it yields on the mode of cavitation attack and 2) by the lack of work that has been carried out on ceramics. The properties of the material will determine the mode of damage and the mode and its severity determine the extent of material removal and strength degradation.

The most important parameters are expected be yield strength, tensile strength, hardness, resilience (ultimate and Hobbs) and strain energy to fracture[37,43]. No work has apparently been undertaken on size effects arising from the scale of the microstructure relative to individual cavitation events. Preece[39] has proposed that cavitation erosion is a more sensitive function of microstructural properties than bulk properties and suggest optimisation of the former by ensuring a small grain size and a ductile mode of erosion. Low cavitation erosion is also found where high work-hardenability is exhibited[35]. Heathcock[37] emphasises

the importance of ensuring a low density of initiation sites and proposes a correlation between flow stress and cavitation erosion.

Although moderate success has been found in correlating the cavitation of metals with their Hobbs[43] or ultimate[44] resilience the calculation of these values for ceramics is more difficult, especially under conditions which simulate those experienced during cavitation erosion. In general there have been no succesful attempts at modelling this type of wear process. Correlations have been found only for small groups of similar materials, and consequently, models have either been too specific in application for any predictive usefulness or have yet to be tested[39].

2.2.4: Effects of transformation on erosion.

Phase transformations in memory alloys, metastable stainless steels, cobalt based tungsten carbide hard metals and Stellites have been found to exert a positive effect on cavitation performance[34,37]. High stacking fault energy discourages transformation and leads to higher rates of cavitation. A transformation is thought to absorb sufficient of the cavitation energy to moderate its effects. Reversible transformation and the possibility of continuous dynamic energy absorption have not been investigated.

CHAPTER 3.

MATERIALS UNDER INVESTIGATION

The group of materials under investigation offers a good range of microstructures and properties. Although the ultrahard materials must be considered within a separate regime for solid particle erosion due to their greater hardness than the erodent, they have not been well investigated before and their response to impact was thought to be likely to provide unique information on their properties and the erosion process in general. It must be noted that only one sample of each material was available for each test. Given the statistical nature of many of the mechanical properties of ceramic materials, and the general variation in materials from batch to batch, especially in experimental materials, caution must be exerted in the direct extension of many of the results to other nominally identical materials.

The erosion performance of the sialon and the zirconias have been evaluated before, but the precise mechanisms of erosion are not as well understood as their present technological importance justifies.

3.1: Ceramic materials

3.1.1. Stabilised zirconias.

Zirconium oxide can be considered to be wholly ionic in nature. It has three major polymorphs. From room temperature to around 1000 degrees centigrade the stable phase has a

baddelyite structure with a monoclinic unit cell. At 1000 degrees centigrade the structure changes to tetragonal. This martensitic transformation is accompanied by a 3-5 per cent volume contraction. At 2280 degrees centigrade the coordination polyhedron becomes regular with a transformation to a cubic unit cell of the fluorite type. This structure persists up to the melting point at 2850 degrees centigrade.

The martensitic tetragonal (t) to monoclinic (m) transformation is catastrophic on cooling due to its associated volume increase in the pure material, but can be used to advantage in two ways provided that transformation can be controlled and triggered heterogenously. This may be achieved by

1) alloying to increase the mean cation radius slightly in order to obtain a suitable radius-ratio for cubic coordination and preclude the t and m phases or

2) the material may be produced in the form of single domain particles below the critical particle size for transformation where the tetragonal form will be stable.

Magnesia, calcia, yttria or ceria are typically used for stabilisation. Both partially- and fully stabilised materials have been tested and are discussed separately below.

3.1.1.1: Partially stabilised zirconia (PSZ)

PSZ is a mixture of cubic and monoclinic (or tetragonal) zirconia that may be formed either by

a) adding insufficient dopant/stabilizer for complete stabilization, or

b) by suitable heat treatment of the fully stabilised material. Production entails firing the green body close to or just inside the single phase cubic phase boundary, followed by isothermal ageing at about 1400 degrees centigrade to develop oblate spheroids (1-2 micron) of the tetragonal phase within the (40-70 micron) cubic grains. A further subeutectoid treatment is often used to improve properties.

The superior mechanical properties of the material derive from two possible mechanisms:

1) If the t (tetragonal) precipitates develop too close to the critical size for transformation during the firing, then upon cooling they will transform spontaneously to the m phase. The 3 to 5 percent volume expansion associated with the transformation results in tangential stresses being set up around the t precipitates. These stresses induce microcracking in the cubic (c) matrix and these microcracks interact with macrocracks propagating through the material by the process of crack bifurcation and concomitant energy absorption. This results in enhanced toughness.

2) If the size of the t particles is kept suitably low then they may be retained down to room temperature by the restraint the matrix imposes on (the dilatational part of) the transformation. Now if a crack extends under an applied stress through the PSZ between the metastable t precipitates, then the large tensile stresses associated with the crack tip will interact with the particles. If the stress is sufficiently large, then it will counteract the restraint of the matrix on the t phase and allow transformation. The associated volume increase and shear strain (1 to 7 per cent) results in a nett compressive stress field in the matrix which restricts crack propagation

and increases the effective energy to fracture and the toughness.

The partially stabilised zirconia (PSZ) that was tested was doped with approximately 10 per cent magnesia. (See fig.3)

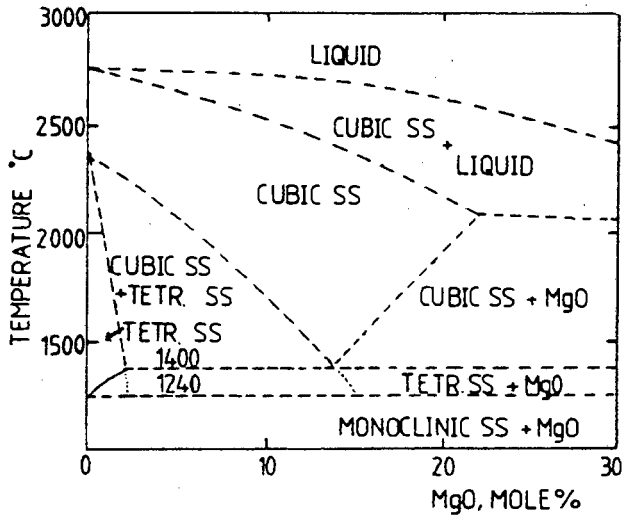

Figure 3. ZrO_2-MgO phase diagram[45].

3.1.1.2: Tetragonal zirconia polycrystals (TZP)

Addition of rare earth oxides in the appropriate amounts with the correct heat treatment can result in complete stabilisation of zirconia. The resultant material has a toughness which is unprecedented in ceramics. The mechanism is identical in principle to the second one above. Cracks propagating through the matrix result in large transformation of material within the process zone and the associated compressive stresses serve to close the crack tip. In addition, grinding of the surface of TZP components causes wholesale transformation and large biaxial compressive stresses on the surface. This acts in a manner which is analagous to the thermal toughening of glass to improve the toughness of the material.

Two modifications of fully stabilised tetragonal zirconia polycrystals have been investigated. The 2 per cent material (2YTZP) was fired at 1575 degrees centigrade for 2 hours and the 3 per cent material (3YTZP) for 1 hour at 1450 degrees. Reference to the yttria-zirconia phase diagram (fig.4) explains the final fine grain and phase structures discussed in the results section below. A small amount of intergranular glassy phase is typically expected in these materials. The materials are expected to exhibit different degrees of transformability due to their different microstructures and heat treatments.

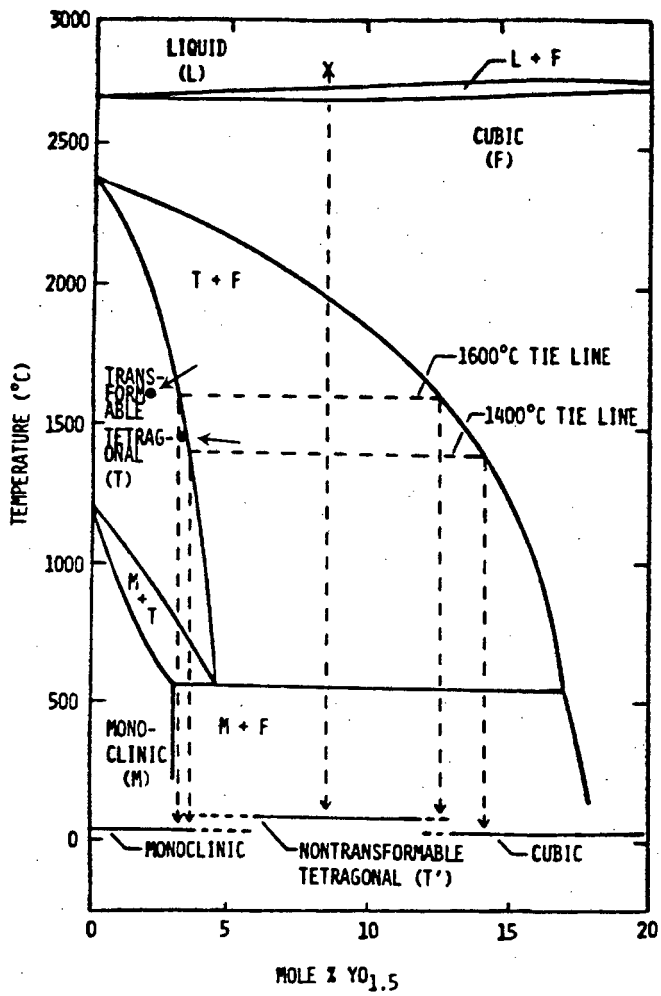

Figure 4. ZrO_2-Y_2O_3 phase diagram[45].

3.1.2.: Sialon:

Sialon is produced by the stoichiometric substitution of aluminium and oxygen into beta-silicon nitride (SI_3N_4) which results in $Si_{6-z}Al_zO_zN_{8-z}$; hence its common name. This results in an excellent combination of the strength and stability of the silicon nitride and the modified chemical properties of the alumina. The latter has important implications for processing and manufacturing since it results in the lowering of the vapour pressure of the compound. This both enables conventional sintering techniques to be used at relatively low temperatures and results in the production of fine homogenous structures. Yttria is used as the sintering aid and a dual phase structure is usually formed where the primary phase is sialon and the secondary phase is determined both by the sintering aid, the degree of stoichiometric substitution and the heat treatment. The material which has been used in this study was sintered with yttria and has a glassy second phase of yttrium aluminium garnet (YAG). This is introduced to enhance retention of strength at high temperatures.

3.1.3: Alumina.

Alumina has a distorted hexagonal close packed layered structure. Its expected ionic nature is perturbed by the small highly charged Al^{3+} ions which result (by Pauling's electronegativity calculation) in a 37 per cent covalent nature. Because of the resultant distortion of the HCP arrangement, large elastic and thermal anisotropy is displayed.

Three modifications of high density, high purity, polycrystalline aluminium oxide have been included in the tests here. This offers several advantages. In the first instance the materials have different grain sizes and

porosities and this has allowed a systematic investigation of the interdependent effects of these variables. These materials are the only truly single phase materials in the investigation which do not have phenomena such as phase transformations complicating their behaviour and this has facilitated their use as simple model materials. Finally, the details of the deformation and fracture of alumina under more tractable conditions than those under investigation here are well characterised.

3.2. Ultrahard materials

3.2.1: Polycrystalline diamond (PCD).

Two modifications of Syndite* have been tested. The materials are manufactured by hot isostatic pressing of a fine (synthetic or natural) diamond grit in the presence of a solvent/catalyst (cobalt) for diamond synthesis. The graded powders are consolidated at pressures and temperatures comparable to those at which they were originally synthesised (1500-2000 degrees centigrade and 5-7 GPa). In the course of the manufacture, plastic deformation of the grit and cobalt takes place. As high temperatures are reached, reconversion of diamond to graphite takes place at the grain surfaces where it diffuses into the catalyst. Reprecipitation causes extensive intergrowth of the grains. The result of this is a contiguous skeletal structure of diamond with cobalt filling the remaining volume. It has the hardness of the diamond matrix but an isotropic toughness superior to diamond itself.

The two modifications used in this study have nominal starting grain sizes of 2 (Syndite 002) and 25 (Syndite 025) microns respectively. PCD002 has 13 and PCD025 11 weight per cent cobalt added as a catalyst respectively.

3.2.2: Polycrystalline cubic boron nitride (PCBN).

Cubic boron nitride (CBN) is the second hardest material known to man and finds applications in aggressive environments of iron or nickel where attack of diamond compacts would occur.

The consolidation procedure is essentially the same as for PCD. The material that has been evaluated here is Amborite* which is sintered in the presence of aluminium. Unlike the case for diamond, the binder does not act as a solvent or catalyst, but reacts with the boron nitride to form a thin AlN skin around the CBN grains and a residual binder phase of aluminium diboride (AlB_2). The superior properties derive not from intergrowth therefore but from the plastic deformation and fracture of the BN due to compaction which results in an effective load bearing structure. The material acts as a true composite material.

The Amborite used here has a nominal grain size of 8 micron and is fully densified. Eighteen weight per cent of aluminium is admixed during manufacture resulting in a final binder content of about 12 per cent.

* Trade names of De Beers Products (see Table 1.)

CHAPTER 4.
EXPERIMENTAL PROCEDURES.

4.1. PREPARATION

All specimens (with the exception of the ultrahard materials) were mounted in perspex and ground to 1200 grit on successively finer silicon carbide papers. The specimens were cleaned in alcohol in an ultrasonic bath and polished on an automatic polisher on diamond impregnated cloth of successively finer grades (15, 7, 2.5 and 0.25 micron). The samples were ultrasonically cleaned between polishing cycles to prevent contamination of the finer cloths.

4.2. CHARACTERISATION

4.2.1: Porosity

Polishing the samples allowed quantization of the porosity in the ceramics. A fine grid was superimposed over large magnifications of optical micrographs of the polished surfaces. Lineal and areal point counting was carried out to ascertain the volume per cent porosity. Porosity is expected to be negligible in the diamond and boron nitrride compacts due to their dual phase nature and their manufacturing techniques.

4.2.2: Grain size determination.

The polished ceramics were etched to determine the grain sizes. Alumina was thermally etched at 1400 degrees centigrade for half an hour while the zirconias and sialon were etched for fifteen minutes in concentrated hydrofluoric acid (HF) at room temperature followed by a rinse in concentrated sulphuric acid for five minutes. Information on the grain sizes and morphology of the ultrahard materials

the grain sizes and morphology of the ultrahard materials was supplied by the De Beers Diamond Research Laboratory.

4.2.3: Mechanical testing.

The ceramics were subjected to indentation in the macro- and microhardness regimes to determine both their hardnesses and indentation toughnesses. An Esseway hardness tester was used to obtain the 30Kgf Vickers macrohardness value while a Shimadzu microhardness machine was used for the determination of the 500g vickers microhardness values. A Nikon optical microscope with a calibrated graticule enabled accurate measurements to be made of the indentation diameter and radial crack lengths. These figures allowed calculation of the hardness of the materials as well as calculation of the indentation fracture toughness by the method of Evans and Charles[46]. Toughness and hardness values for the ultrahard materials could not be obtained on the available apparatus but have been measured by Lammer[47].

4.2.4: Energy Dispersive Spectroscopy.

A Tracor Northern system installed on a Cambridge 200 scanning electron microscope was used

1) to determine whether the sintering aid used in the manufacture of the PSZ was magnesia, yttria or calcia and

2) to determine as accurately as possible the chemical nature of melting features observed during the solid particle erosion of alumina. This latter investigation was undertaken to try and ascertain the mechanism and extent of thermomechanical heating taking place at an impact site.

4.3. SOLID PARTICLE EROSION

4.3.1 Erosion rig.

A conventional gas blasting type of apparatus was used for the solid particle erosion. The size of the erosive silicon carbide particles was narrowly confined to 120 grit by sieving. This corresponds to an average particle diameter of about 150 micrometers. Particles are extremely angular as may be seen by reference to figures 27 and 28. The double rotating disk technique of Ruff and Ives[48] was used to set up a calibration curve between air pressure and particle velocity. This allowed the particle velocity to be accurately controlled and it was set at 40 metres per second for the duration of these tests.

4.3.2: Single impacts and steady state testing.

In order to determine the mode of material removal and damage initiation, a very small amount of silicon carbide grit was initially blasted at the targets to facilitate the scanning electron microscopical investigation of the morphology of single impact sites. The ceramic specimens were subsequently repolished and all the specimens were subjected to successive blasts of 5 gram batches of silicon carbide. In between cycles, the materials were ultrasonically cleaned, dried and weighed on an analytical balance to determine the mass loss. This was converted to a volume loss which was normalised with respect to the amount of silicon carbide grit that had caused the loss. Erosion was continued until it was certain that a steady state situation had been reached.

4.3.3: Dislocation substructure.

Transmission electron microscopy was beyond the scope of this project, but it was deemed important to gain at least a qualitative understanding of the plastic processes occuring beneath an impact site. It was decided therefore to choose a model material which could be etched to reveal dislocation etch pits. A single crystal of LiF cleaved along its <100> directions was chosen for this purpose. The material is cubic and slips in <110> and <100> directions on the six {110} planes.

The sample was subjected to a small number of impacts by 120 grit diamond powder under the same conditions as the other erosion tests. It was ultrasonically cleaned and then etched in hydrogen peroxide for five minutes to reveal the dislocations that had been injected into the almost defect free crystal.

4.4: CAVITATION EROSION.

4.4.1: Cavitation erosion rig and procedure.

Tests were carried out under distilled water at 25 degrees centigrade using an ultrasonic drill driven by a magnetostrictive oscillator in close proximity to the specimen. The stationary specimen configuration as described by Vyas and Preece[40] was used (fig. 5). The amplitude of the oscillation of the horn tip was set to resonance at 75 micron and the frequency was set at 20 KHz. These parameters were monitored by an instrumented stylus attached to the horn.

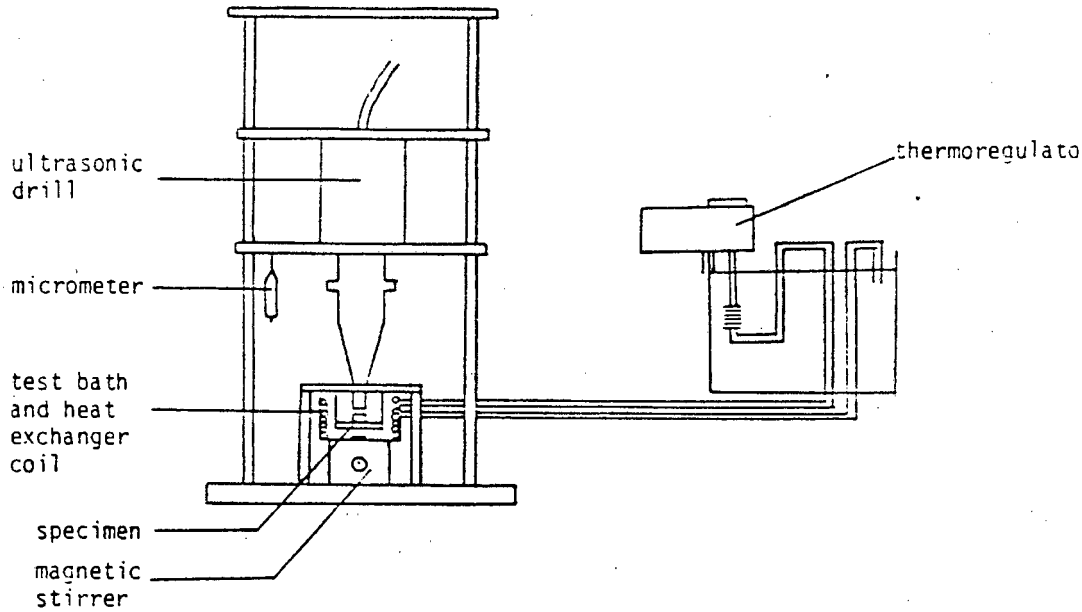

Figure 5: Cavitation erosion apparatus.

The ceramics were polished before testing while new as-received samples of the ultrahard materials were used. Specimens were initially subjected to cavitation for a very short time and then examined to determine the modes of damage initiation. After this they were cavitated for periods of one hour at a time and finally 5 hours at a time until it was certain that steady state erosion had been established. Between cycles, the materials were cleaned and weighed on an analytical balance to determine their mass losses as a function of time of exposure to the ultrasonic drill. These losses were again converted to volume losses.

4.5: MICROSCOPY.

4.5.1: Optical microscopy.

A Nikon optical microscope was used to investigate the dislocation structure beneath the impact sites on the single crystal of LiF.

4.5.2: Scanning electron microscopy.

The small scale of the damage induced in the materials both by cavitation and solid particle erosion required that electron microscopy be used to resolve the details adequately. A Cambridge 200 scanning electron microscope was used to investigate the initial stages of both solid particle and cavitation erosion and also the steady state surfaces. All the ceramic and ultrahard materials were sputtered with gold-palladium on a Polaron coater to ensure that charging of the samples did not take place under the beam. In addition the diamond compacts had to be demagnetised to reduce astigmatism induced by the presence of cobalt in the samples.

4.6: X-RAY DIFFRACTION.

Changes in structure in a polycrystalline material may be readily observed using x-ray techniques. In order to investigate the effects of erosion on the stress induced transformation in the stabilised zirconias, x-ray diffraction was undertaken. A Phillips Diffractometer with a copper-tube was used to obtain traces of the as-polished and as-eroded surfaces of the three zirconias. This allowed the determination of the relative ratios of tetragonal to monoclinic phases in the polished and damaged states. The scanning variables were chosen to optimise the peaks of interest.

CHAPTER 5.

RESULTS

5.1: CHARACTERISATION OF MATERIALS.

Table 1 presents the measured grain sizes, porosities, hardnesses and toughnesses of the ceramic materials under investigation. Other relevant properties of the ceramics and the properties of the ultrahard materials are also presented in this table. These latter properties have either been collected from the literature or have been supplied by the manufacturer.

TABLE 1 : Summary of Material Properties and Performance.

MATERIAL	CODE AND TRADENAME	DENSITY (g/cm^3)	POROSITY (per cent)	GRAIN SIZE (micron)	MODULUS (GPa)	HARDNESS (20 kgf)	STEADY STATE PARTICLE EROSION RATE $cm^3 \times 10^{-5} g^{-1}$	STEADY STATE CAVITATION EROSION RATE $cm^3 \times 10^{-5} hr^{-1}$
ALUMINA	A17	3,87	5,0	5,3	380	1396	16,2	230,0
ALUMINA	A16	3,94	2,2	2,6	380	1750	7,3	23,1
ALUMINA	R	3,98	1,5	1,5	380	1892	5,8	13,9
PARTIALLY STABILISED ZIRCONIA	PSZ	5,7	3,9	35,0	205	1049	10,2	1,5
TETRAGONAL ZIRCONIA POLYCRYSTAL	2YTZP	6,0	2,4	0,8	207	1505	5,8	2,8
TETRAGONAL ZIRCONIA POLYCRYSTAL	3YTZP	6,1	1,4	0,2	208	1585	4,9	2,6
Si-AL-O-N CERAMIC	Syalon 201*	3,3	3,2	0,5	288	1584	5,2	4,4
POLYCRYSTALLINE CUBIC BORON NITRIDE	PCBN Amborite**	3,4	18 (Al)***	8,0	680	3200	0,6	2,9
POLYCRYSTALLINE DIAMOND	PCD002 Syndite**	4,2	10-13(Co)***	2,0	749	5000	0,01	1,6
POLYCRYSTALLINE DIAMOND	PCD025 Syndite**	3,9	8-10(Co)***	25,0	810	5000	0,1	1,4

* = Trade Name, product of Lucas-Cookson (Pty) Ltd
** = Trade Name, product of De Beers Industrial Diamond Division (Pty) Ltd
*** = Binder content, no porosity

5.2: SOLID PARTICLE EROSION.

5.2.1: Lithium fluoride.

Eroded and etched surfaces of LiF are presented in fig.6 below. Dislocation etch pits are visible, showing the dislocation structure that has resulted from the impact, and the slip systems on which the dislocations glide. The slip systems and crystal orientation are marked.

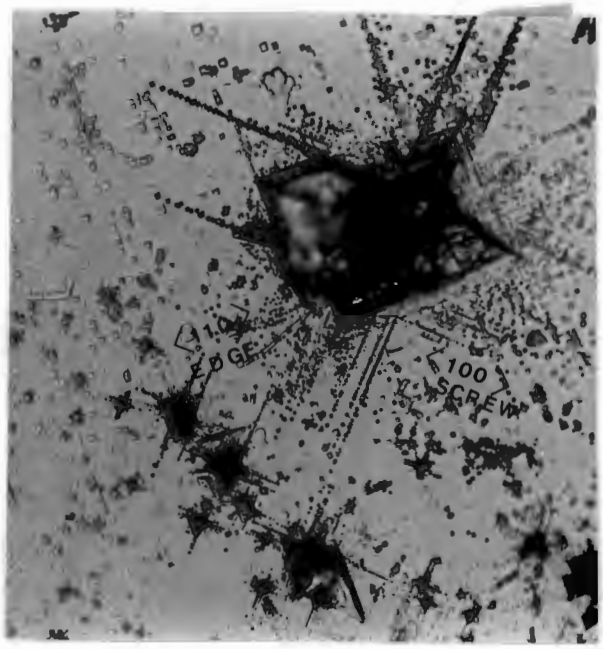

Fig.6 Eroded and etched surface of LiF single crystal. Note the extent of plasticity relative to fracture, and the interaction between crystallographic orientation and orientation of angularity of impinging particle. The particle angularity is of course reflected in the shape of the indentation.

5.2.2: Ceramic materials.

Figures 7-20 present representative micrographs of single impacts and the steady state solid particle erosion morphology of the ceramic materials tested. Important details are pointed out on the individual micrographs. It should be noted that the scale of the fine details of particle-target interaction is a complex function of the particle and target properties and the target microstructural scale. Consequently the magnifications of the photographs are not all the same and this should be taken into account when comparing the performance of different materials.

Fig.7 Single impact on alumina R: irreversible plastic indentation is accompanied by inter-granular lateral venting and median-radial cracking.

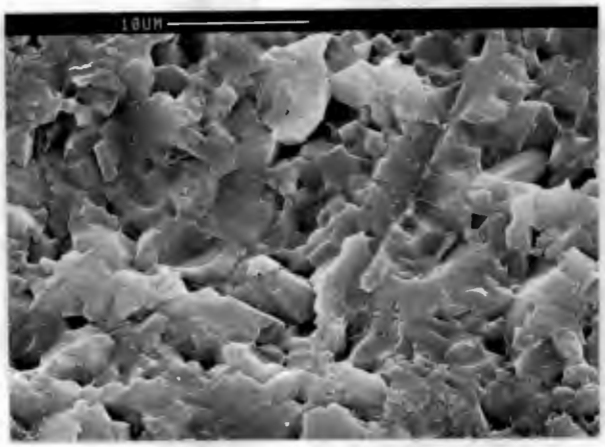

Fig.8 Steady state erosion surface of alumina R: evidence for plastic compaction and some intergranular spallation.

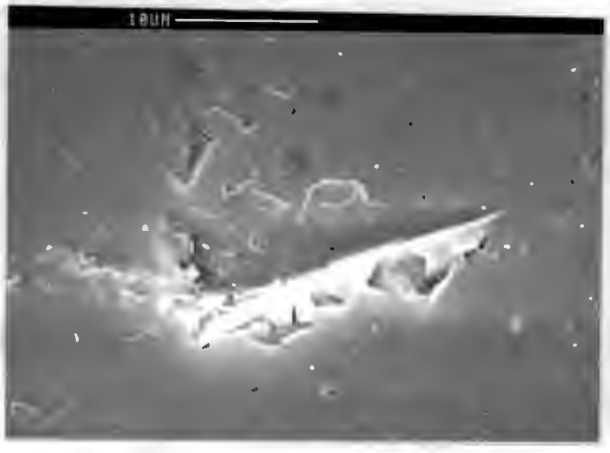

Fig.9 As for fig.7 above but alumina A16

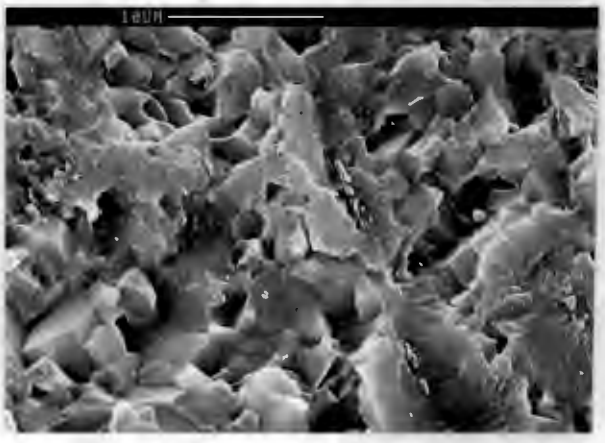

Fig.10 Steady state erosion of A16: greater relative ratio of spallation to plasticity.

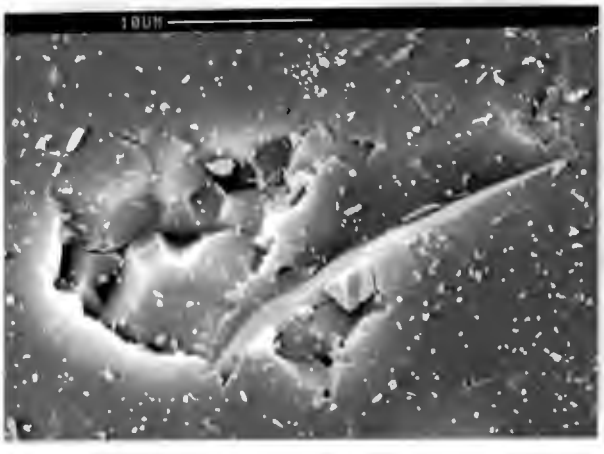

Fig.11 As for fig.8 Alumina A17.

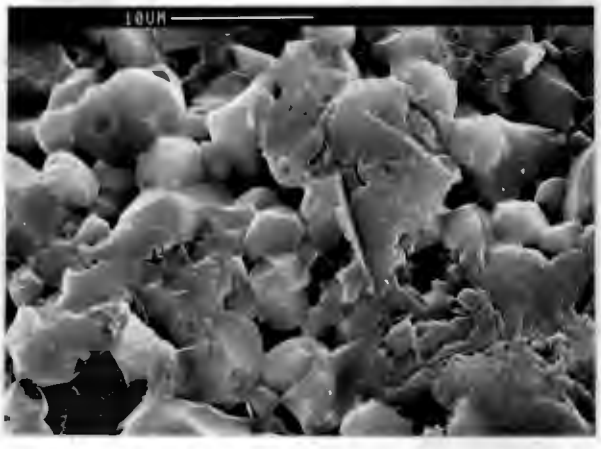

Fig.12 A17: steady state erosion showing large degree of fracture.

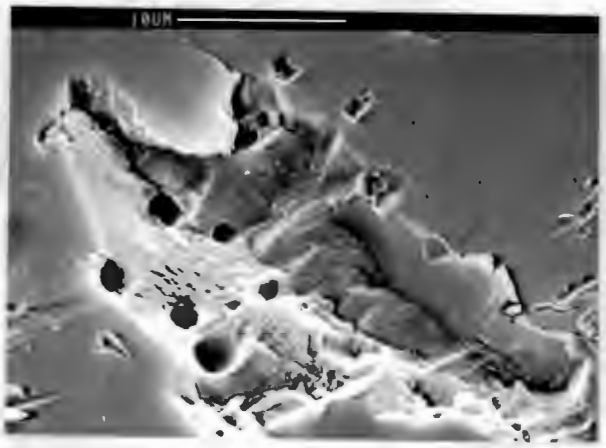

Fig.13 Impact site on PSZ. Fracture is transgranular and conchoidal. Note porosity.

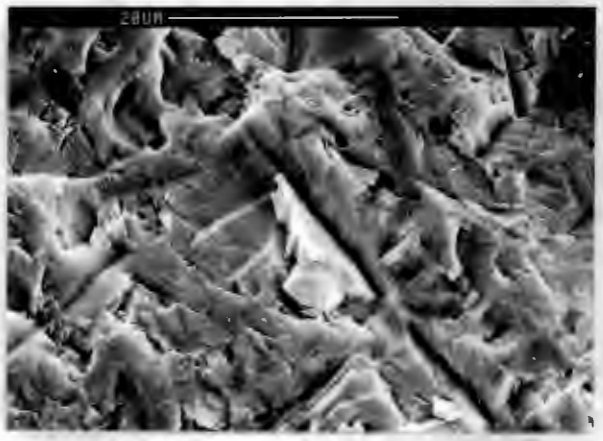

Fig.14 Steady state erosion of PSZ. Some plasticity is evident with a large amount of fracture.

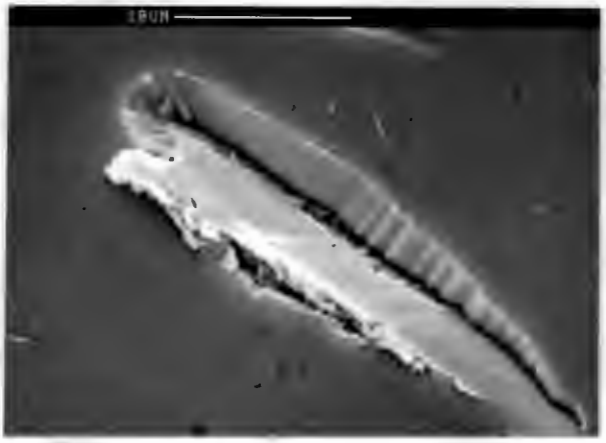

Fig.15 2Y%TZP: indentation is very plastic, and little material removal is apparent. Note the slight rumpling around the impact site.

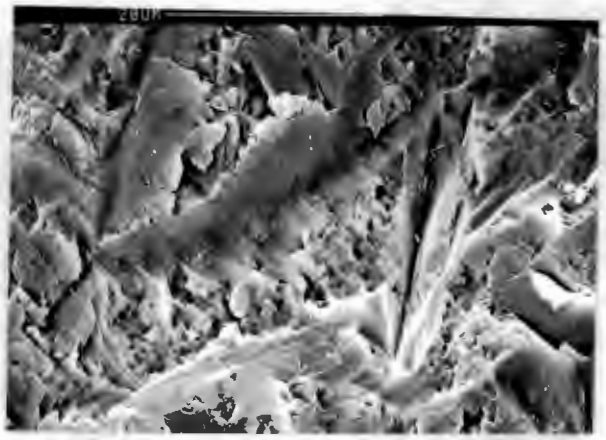

Fig.16 Steady state morphology of 2Y%TZP. Highly plastically deformed, with platelet formation and delamination.

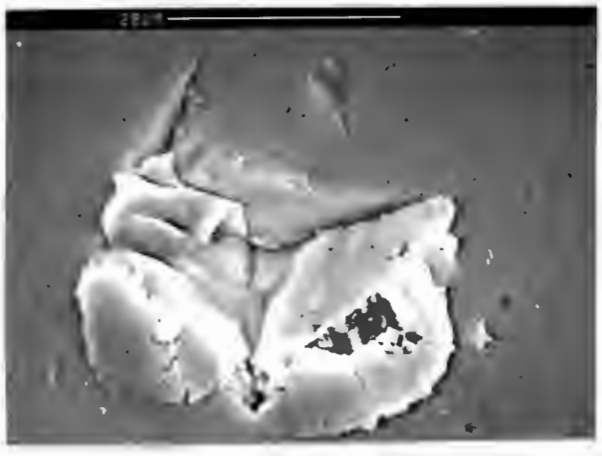

Fig.17 3Y%TZP: Similar to fig.15 above. Well formed lateral vents are evident.

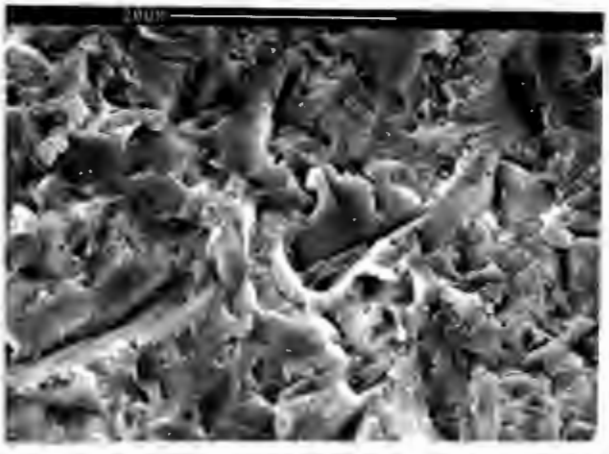

Fig.18 Steady state in 3T%TZP. The morphology is apparently identical to 2Y%TZP.

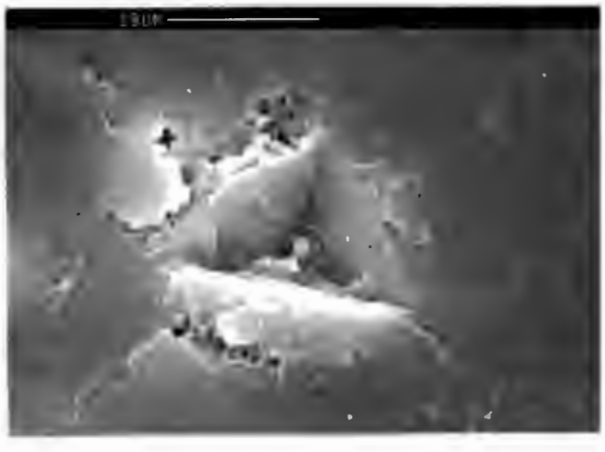

Fig.19 Single impact on syalon 501.The fine grained dual phase material seems quite plastic and resistant to microcracking.

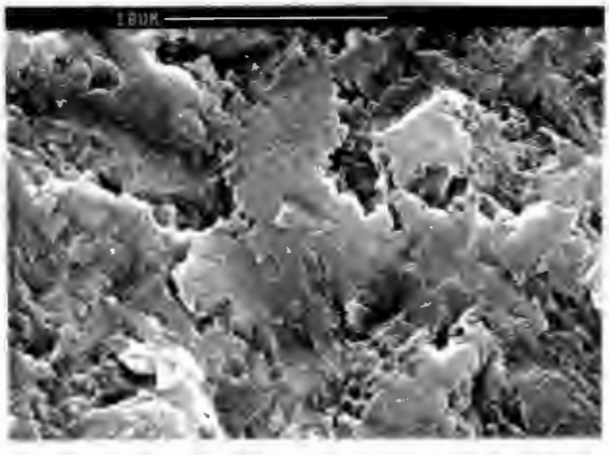

Fig.20 Extremely plastic steady state erosion of syalon, showing platelets and delamination.

5.2.3: Ultrahard materials.

All the ultrahard materials, being harder than the the impinging SiC grit, are significantly resistant to the erosive impact. This superior hardness precludes the possibility of polishing large sections of the ultrahard materials so that these were tested in the as-recieved condition. This condition results from mechanical lapping and has a thin smeared layer of the binder material over the hard matrix. Identification of single impact sites on such surfaces is extremely difficult. For this reason , the as recieved surfaces are presented for comparison with the steady state in figures 21-26.

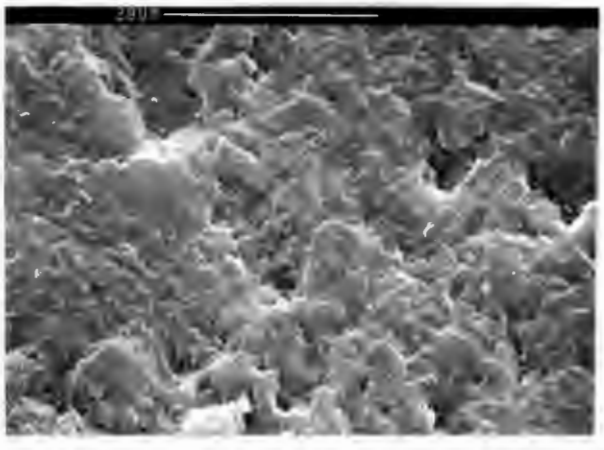

Fig.21 As recieved surface of PCBN. No details of the microstructure can be seen.

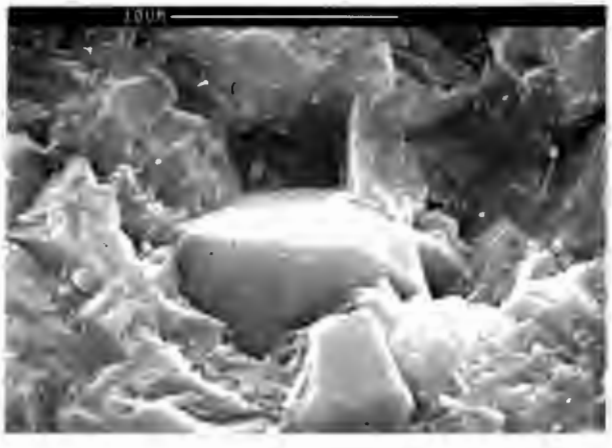

Fig.22 Steady state erosion surface of PCBN. The binder (AlB_2) has been deformed and extruded removing the support of the hard grains. These are then knocked off the surface.

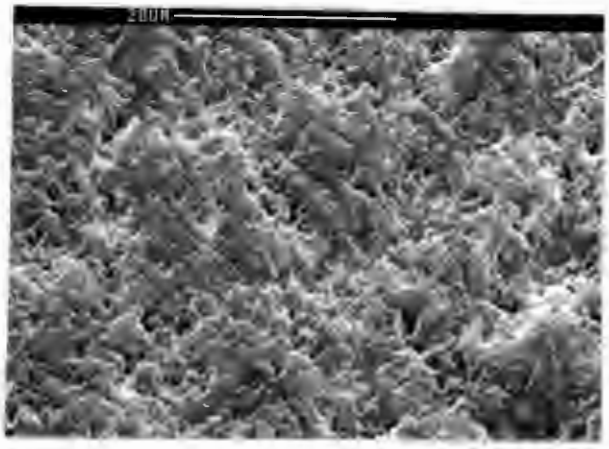

Fig.23 As recieved surface of 002. Cobalt smeared over diamond matrix. No impacts evident.

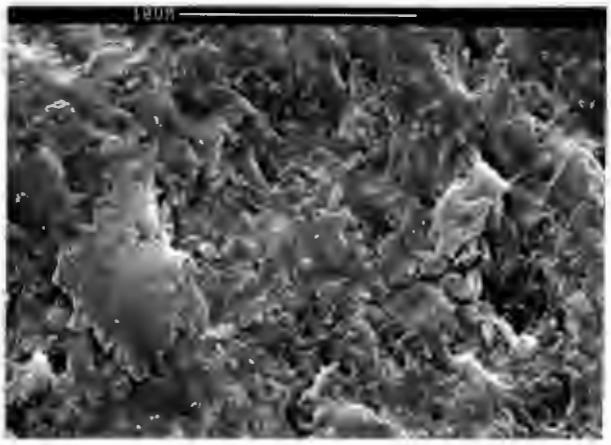

Fig.24 There is no clear evidence of damage in the steady state erosion of PCD002.

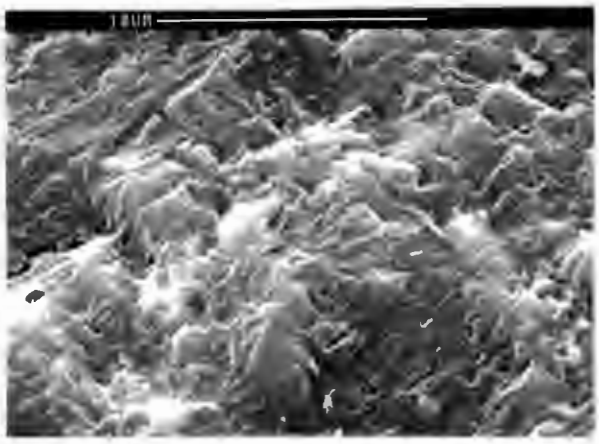

Fig.25 025 as for fig.23 above

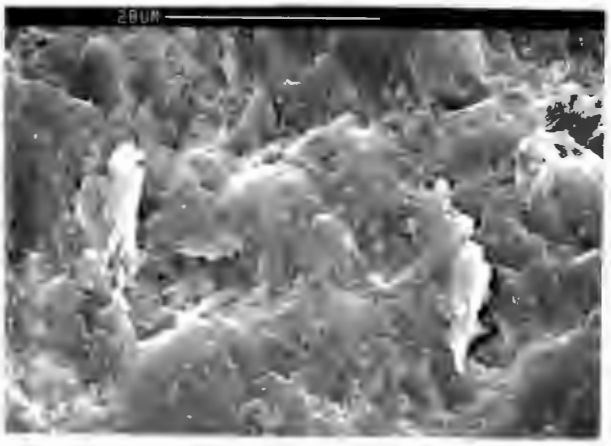

Fig.26 In the larger grained 025, there are larger pools of free cobalt and some of these are accessible to the impacting particles. Extrusion is evident, and this accounts for the small measured mass losses.

5.2.4: Silicon carbide grit.

Micrographs of virgin and used grit are presented below. These reflect the angularity of the particles and also show the conchoidal chipping that occurs on impact. This will be expected to absorb a small amount of the energy of impact.

Fig.27 Virgin SiC grit.

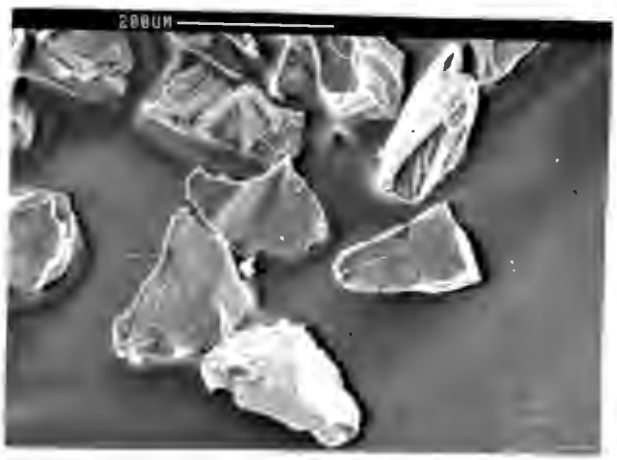

Fig.28 Used grit after erosion of sialon. Note chipping.

5.2.5: Adiabatic melting during the erosion of alumina.

Some 5 percent of impact sites on alumina exhibit features that suggest that melting has taken place, both in single impacts and during the steady state. The figures below indicate typical features of this type.

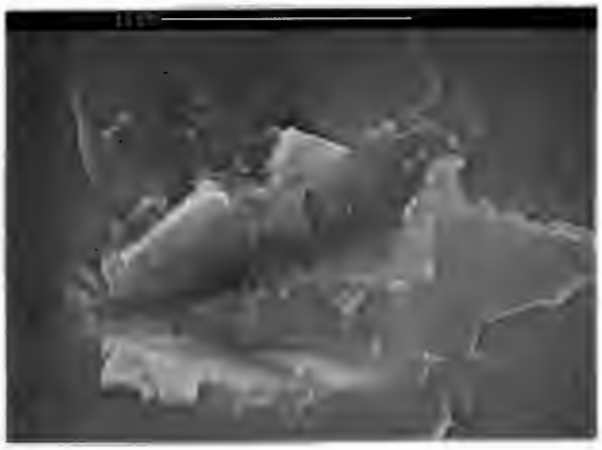

Fig.29 Small droplets of material in an impact site on alumina A16.

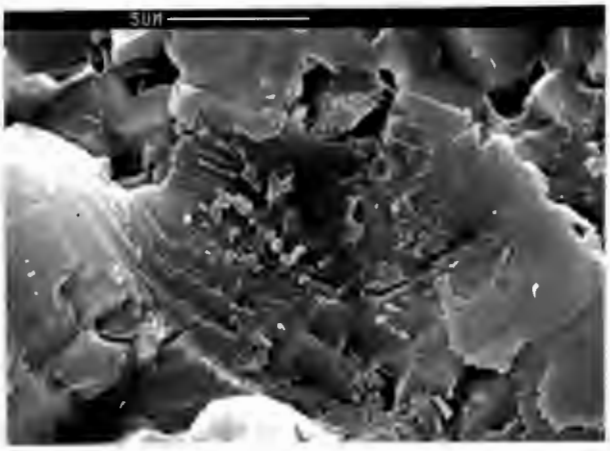

Fig.30 Elongated stringers and globules at an impact site during steady state erosion of alumina A17.

EDS analysis of these features indicates that they contain silicon. Figure 31 shows a trace of a typical spectrum of melting features, while table 2 presents the results of a semi-quantitative analysis of the acquired spectrum, and also gives the acquisition conditions. The values in the table are not accurate because the sampling volume and escape depth are both much greater than the dimensions of the melting features.

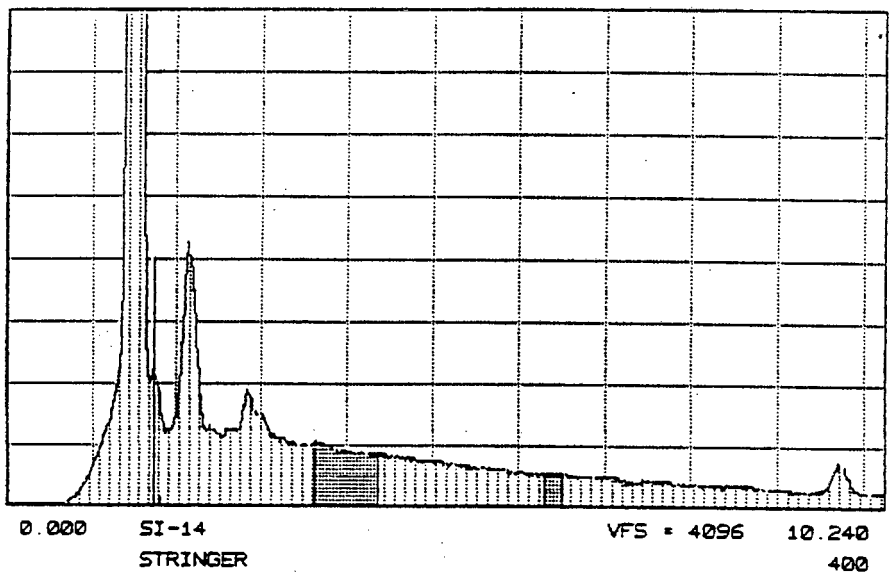

Fig.31 EDS analysis of melting features in alumina R. Note the presence of the silicon peak.

	Si	Al
k	0.004-0.033	0.777-0.846
Z	0.934-0.938	0.966-0.970
A	2.293-2.430	1.147-1.178
F	0.999	0.998-0.999
weight %	0.87-5.92	72.87-81.44
atomic %	0.99-6.98	89.08-95.84

Take off angle: 58.0 deg.
Window: Be (8.4) micron
Si (Li drifted detector)
Dead time: 28

Acc.voltage: 20kV
Working dist: 25mm
Resolution: 6
Magnification:80-110kX

Table 2: Semi quantitative analysis of elemental composition of melting features on alumina R. The conditions used on the TN-5400 x-ray analysis system are also included above.

5.2.6: Evaluation of erosion resistance.

Figure 32 below shows the cumulative volume losses of the materials tested as a function of the mass of erodent impinged upon the target. For clarity of presentation, only alumina R is included. The erosion rates of A16 and A17 are an order of magnitude greater. Note that PCBN is the only material that has a response that is not linear with mass of erodent, and a slight incubation period is indicated.

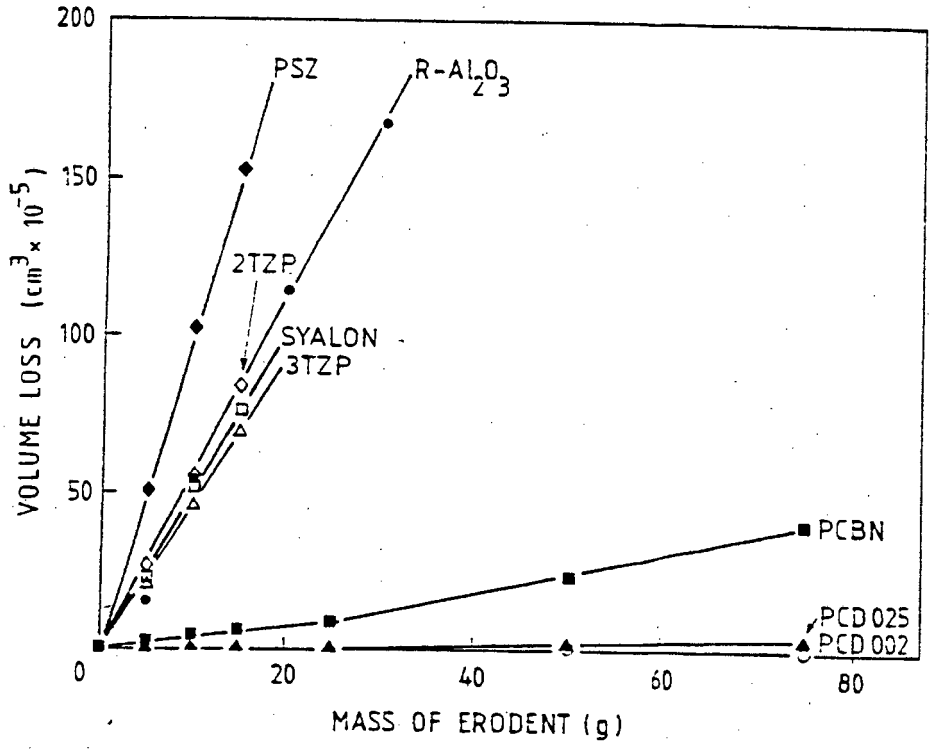

Fig.32 Volume loss of material as a function of the mass of erodent that has impinged upon the target.

The steady state erosion rates for the materials are shown in figure 33. The normalised hardness values are included for comparison and it must be noted that the hardness of the silicon carbide grit lies between the values for the ceramic and ultrahard groups of materials. It is obvious from this that the superhard materials must be considered within a different regime of solid particle erosion.

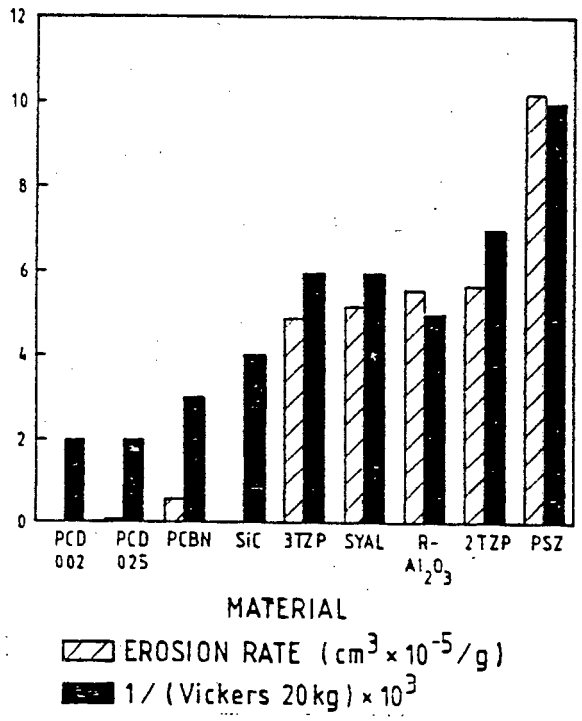

Figure 33: Erosion rates and normalised hardness values for materials under investigation. The hardness value of the silicon carbide particles is included.

Figures 34-38 show the performances of the materials in solid particle erosion versus the properties of hardness, toughness, Youngs modulus, grain size and porosity. It will be noted that good correlations exist between erosion rate and hardness, and between grain size and porosity for the ceramic materials. Only moderate correlation with toughness

and modulus is exhibited. It is clear that the superior hardness, toughness and modulus of the ultrahard materials is relates to their excellent performance.

Two other important features are seen in the figures. Figure 35 suggests that an inverse correlation between toughness and erosion rate exists for the alumina materials. This is discussed in chapter 6 below.

Further, it must be noted that the property-performance relationships for the stabilised zirconia materials are anomalous in general. This is most obvious for the properties of hardness and modulus, where the zirconias show smaller erosion rates than those which might have been expected purely on the basis of their intrinsic properties relative to the other materials.

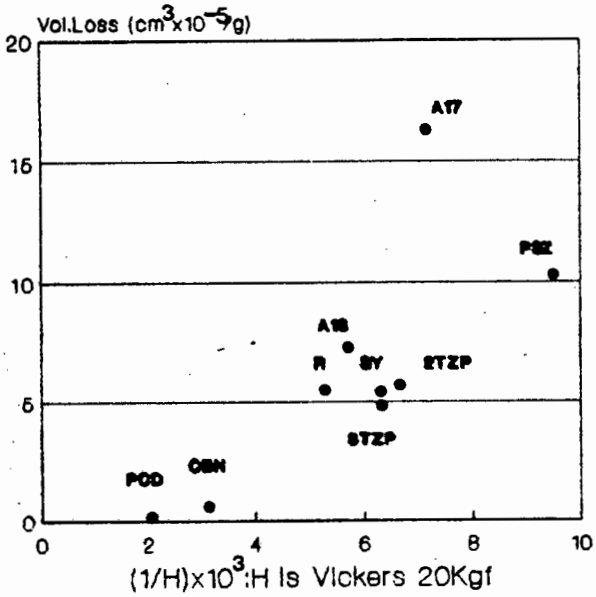

Fig.34 Solid particle erosion versus the inverse of hardness.

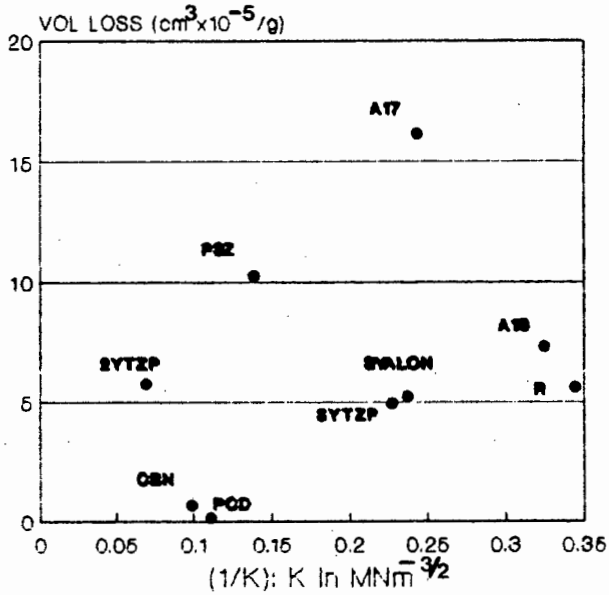

Fig.35 Solid particle erosion versus the inverse of toughness.

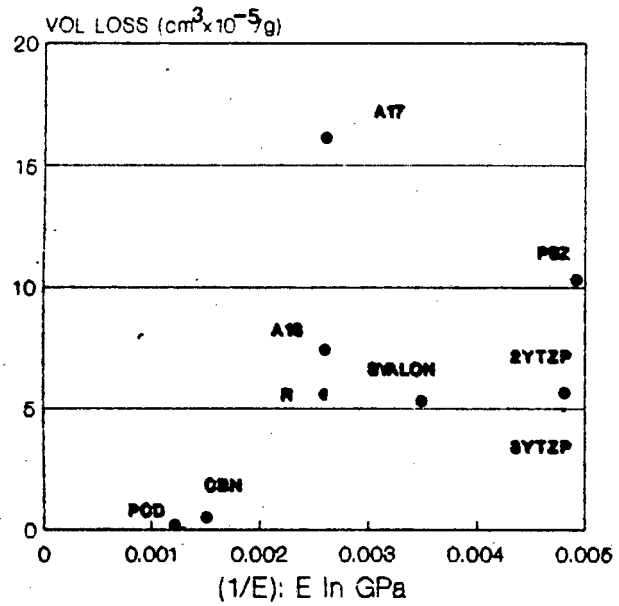

Fig.36 Solid particle erosion versus the inverse of modulus.

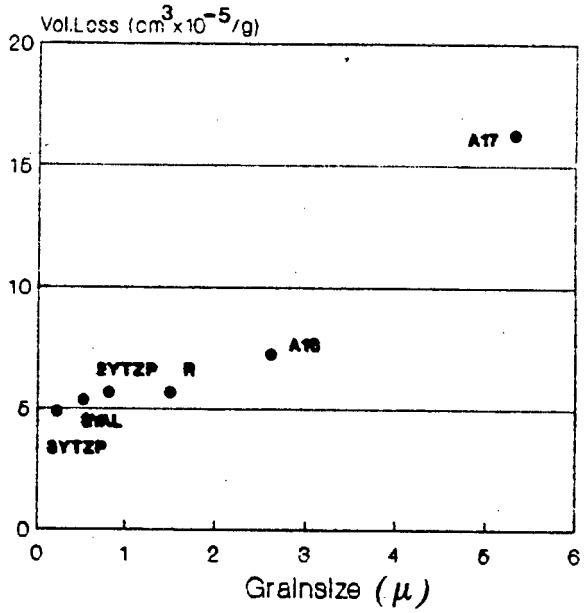

Fig.37 Solid particle erosion versus grain size for the ceramic materials.

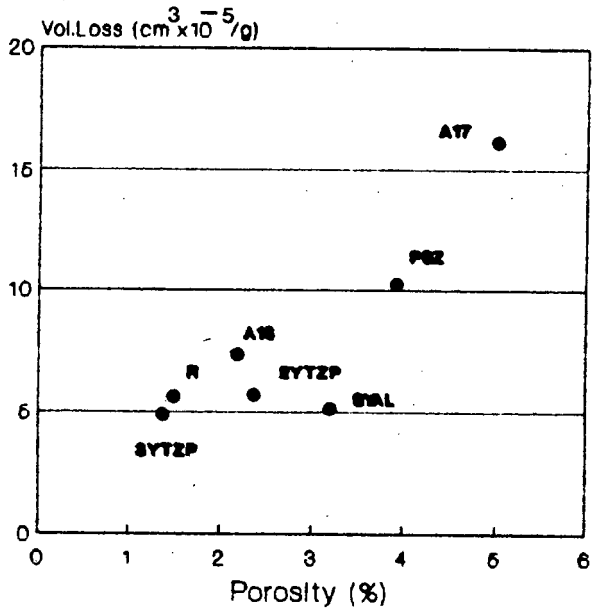

Fig.38 Solid particle erosion versus percentage porosity for the ceramic materials.

5.3: CAVITATION EROSION.

In contrast to solid particle erosion, it is not possible to distinguish the effects of single cavitation events from the wear surface. The figures 39-58 below show representative micrographs of the initiation of damage in the materials (during the incubation period) and the steady state damage morphology.

5.3.1: Ceramics.

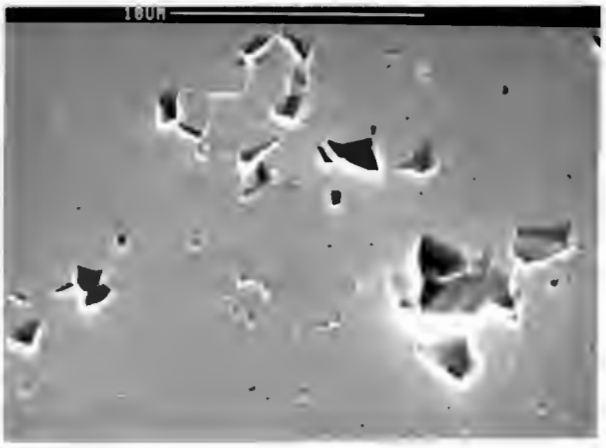

Fig.39 Initiation of damage in aluminr R: intergranular micro-cracking, assisted by porosity.

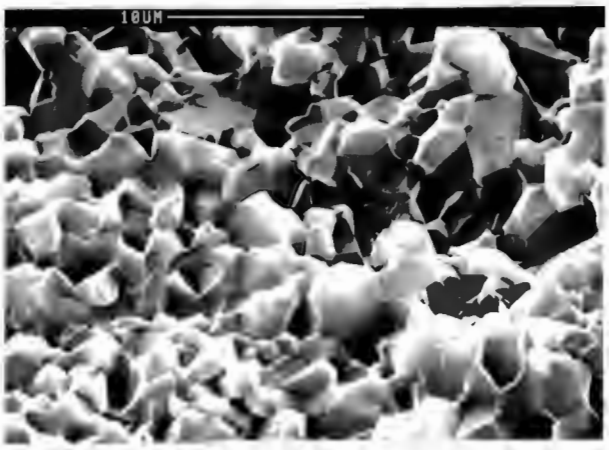

Fig.40 Steady state erosion of alumina R.

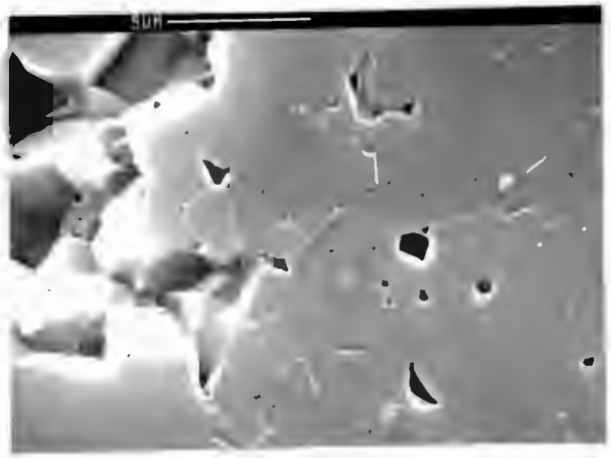

Fig.41 As for fig.39 above but for alumina A16.

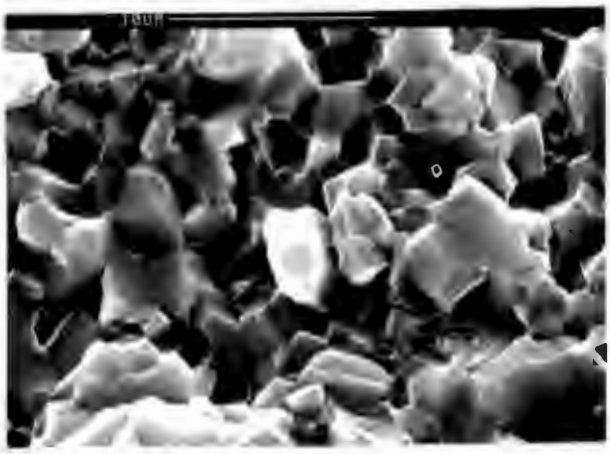

Fig.42 As for fig.40 above, but for alumina A16.

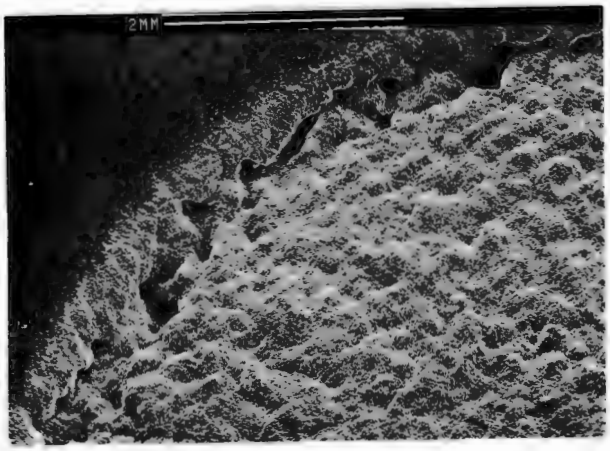

Fig.43 Initiation of damage in A17 is identical to the other aluminas (figs.39 and 41 above). The macroscopic steady state surface of A17 is presented instead showing pit instability.

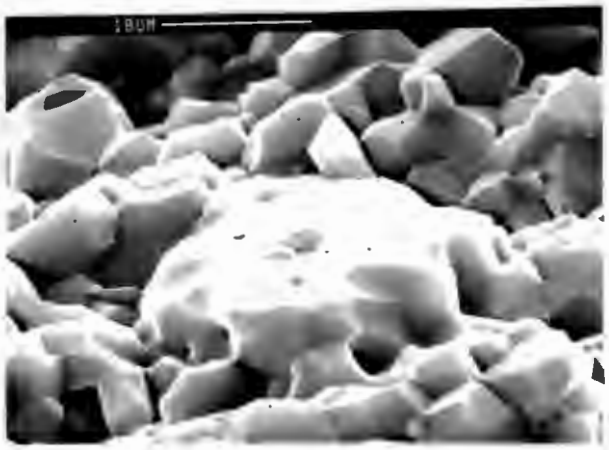

Fig.44 High magnification view of fig.43 on the left: Steady state erosion of alumina A17.

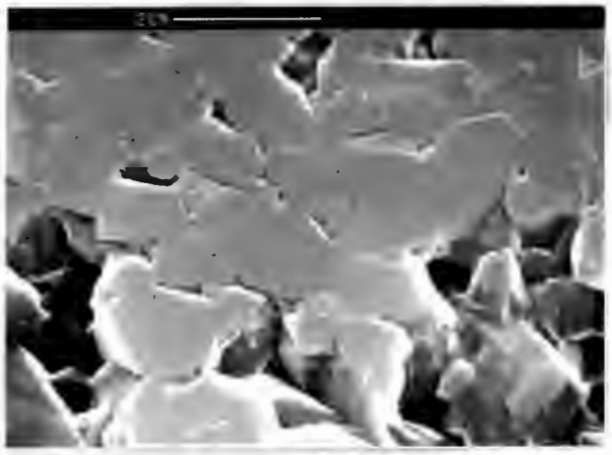

Fig.45 Damage initiates in sialon at the porosity and by preferential attack of the glassy YAG phase.

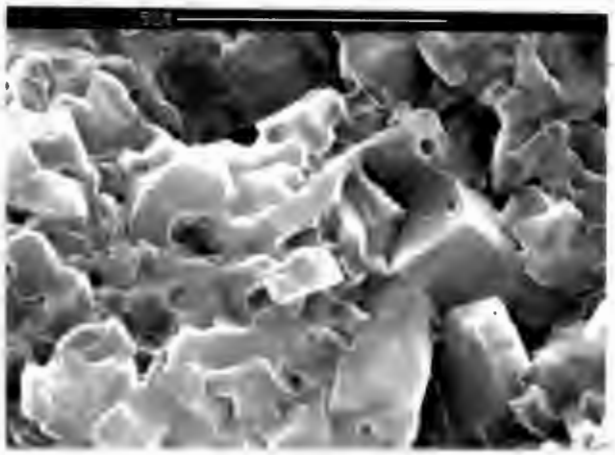

Fig.46 Good cohesion is shown between the grains of sialon during steady state. Note high aspect ratio of grains.

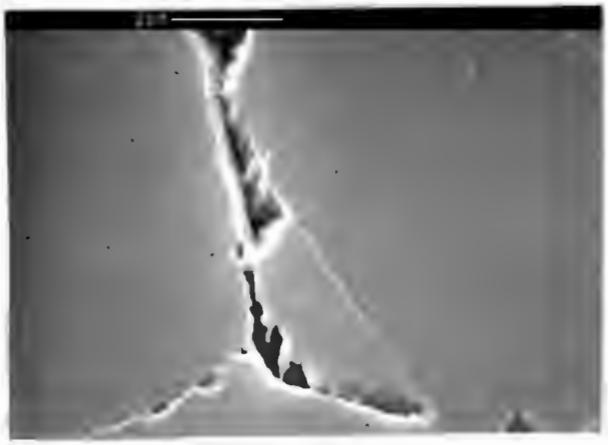

Fig.47 PSZ: initiation in the large grain sized material takes place at grain boundaries and is also very sensitive to extrinsic defects.

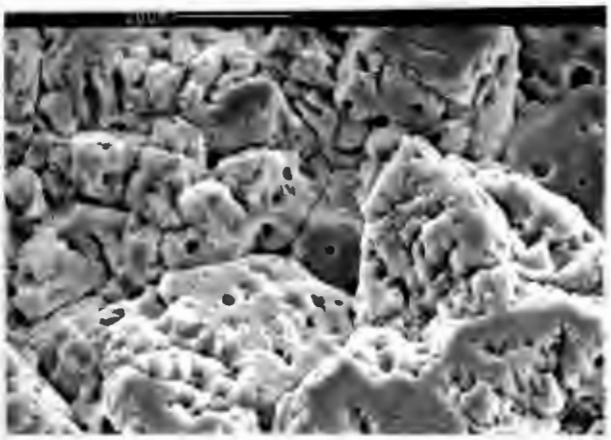

Fig.48 The steady state in PSZ is characterised by transgranular attrition.

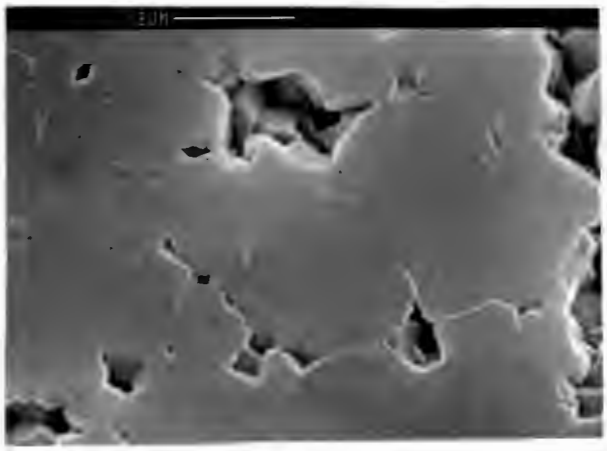

Fig.49 2Y%TZP: the damage initiates at pores and spreads by intergranular microcracking. There is no direct evidence of any transformation.

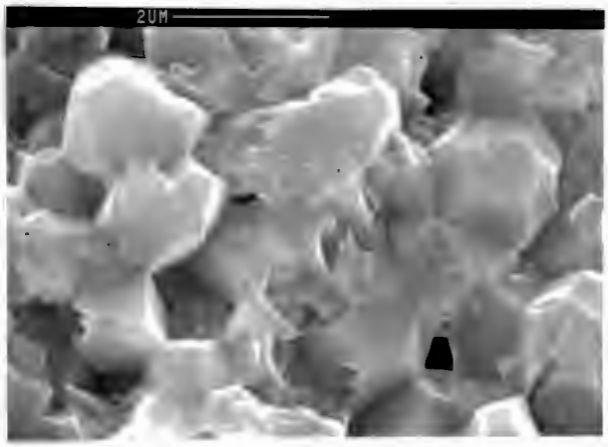

Fig.50 Steady state in the 2Y%TZP is intergranular. Note the small amount of intergranular glassy phase.

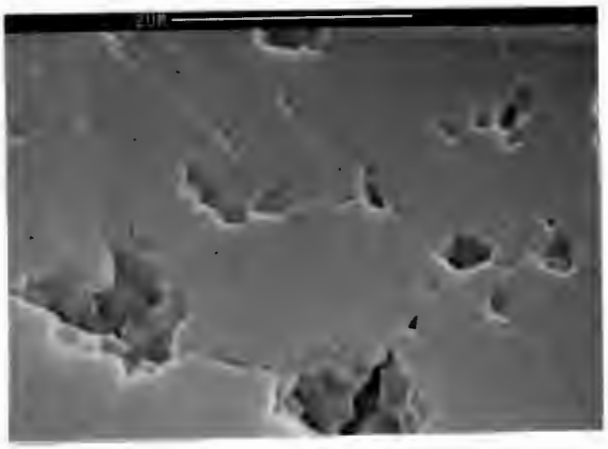

Fig.51 As for 2Y%TZP above. Note the fine grain size.

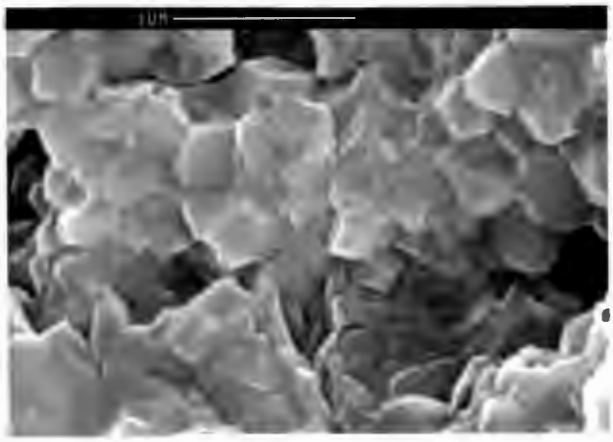

Fig.52 Steady state damage in the 3Y%TZP is as for the 2% material above.

5.3.2: Ultrahard materials.

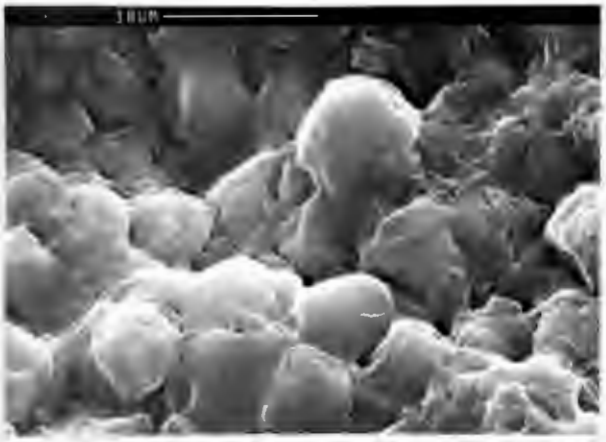

Fig.53 PCBN: damage begins by work hardening and removal of binder phase.

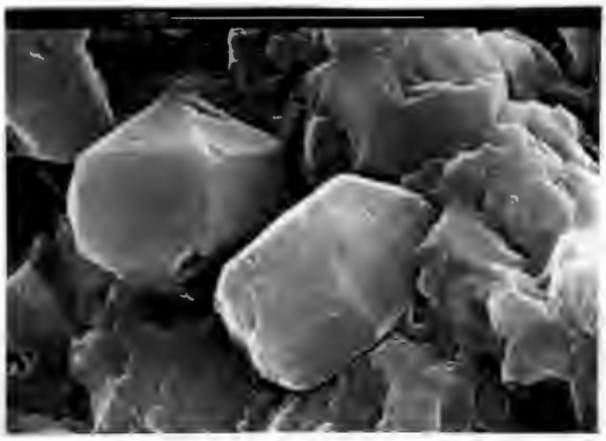

Fig.54 Steady state occurs when binder is removed to the extent that the hard grains are no longer supported and these then spall off. Note the lack of intergrowth.

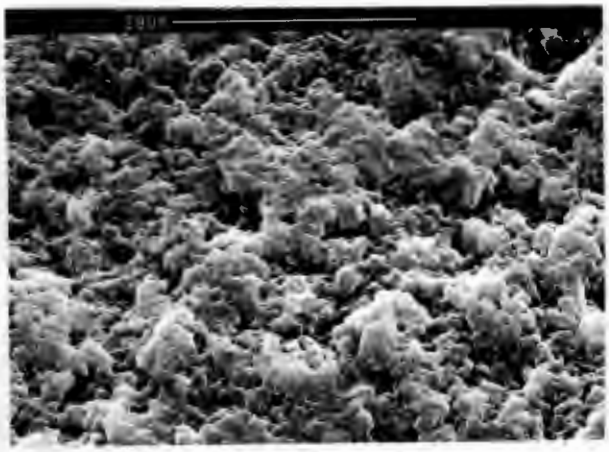

Fig.55 Incubation in PCD 002. The smeared cobalt layer on the surface is removed, and some removal of the inter-granular cobalt begins.

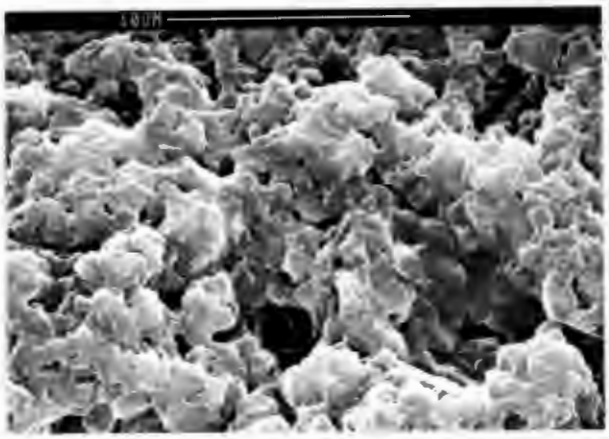

Fig.56 Steady state of PCD 002: Areas where cobalt has been removed act as stress concentrations. Weakly intergrown grain necks can then fracture resulting in material loss.

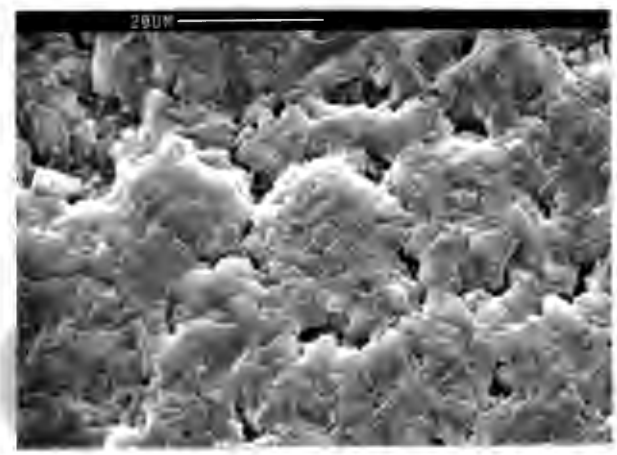

Fig.57 Initiation in PCD 025:cobalt is slowly eroded.

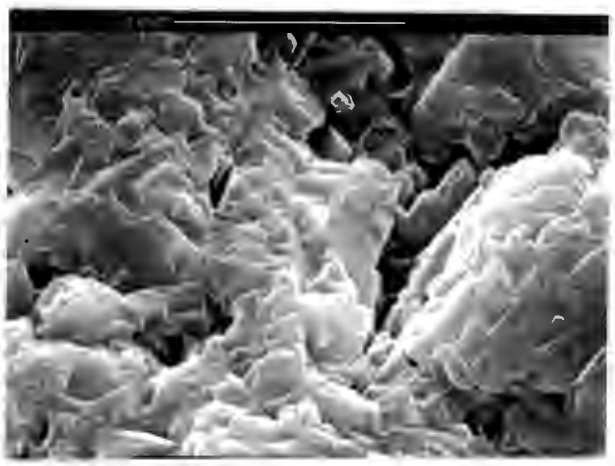

Fig.58 Some grains are removed, but the structure is quite coarse relative to the scale of the erosion events, so that it takes several events to remove any single grain.

5.3.3: Cavitation erosion performance.

The losses of the materials under investigation are presented as a function of time of cavitation in figure 59 below. Attention should be paid to the different forms of incubation that different materials display. The PCD materials display erosion curves which have the opposite second derivatives to the slopes of the other materials; erosion starts off fast and then slows down so that an "inverse incubation" is displayed. It should be noted that with the exception of the PCD's and PSZ to a lesser extent, the steady state erosion rates scale approximately with the incubation period. Longer incubation times are associated with lower steady state erosion rates.

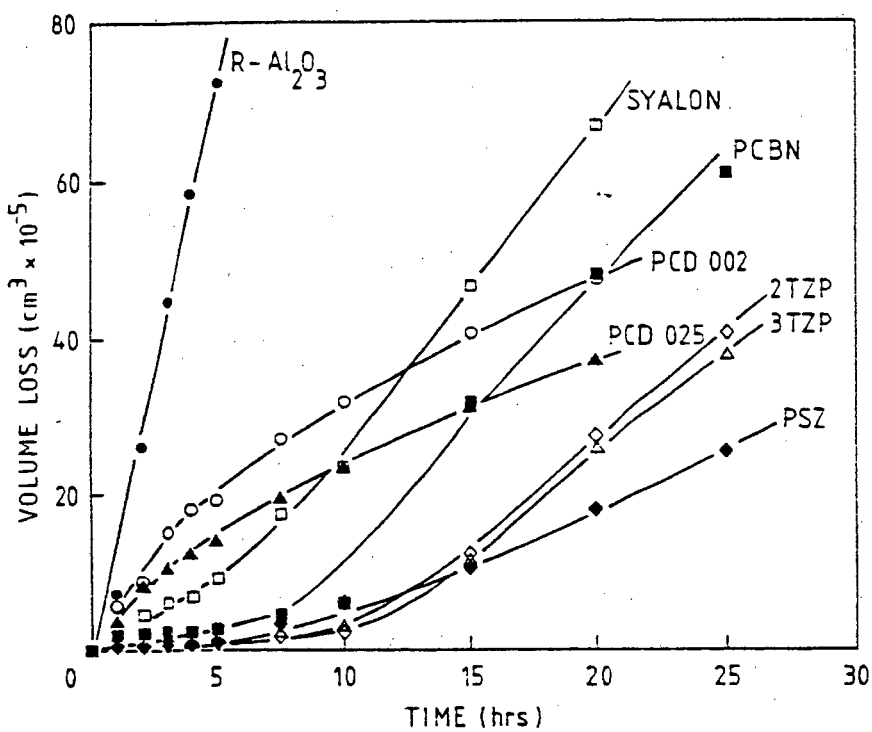

Fig.59 Cavitation erosive volume loss as a function of time. Note the different forms of incubation.

Figure 60 shows the steady state erosion rates of the the samples and the inverse material hardnesses are included for comparison. Clearly there is no correlation in contrast to solid particle erosion. The ultrahard materials again perform well, but not as well relative to particle erosion. Very low erosion rates are also exhibited by the zirconias, while the erosion rates of the other two aluminas were extremely high and have been omitted for clarity.

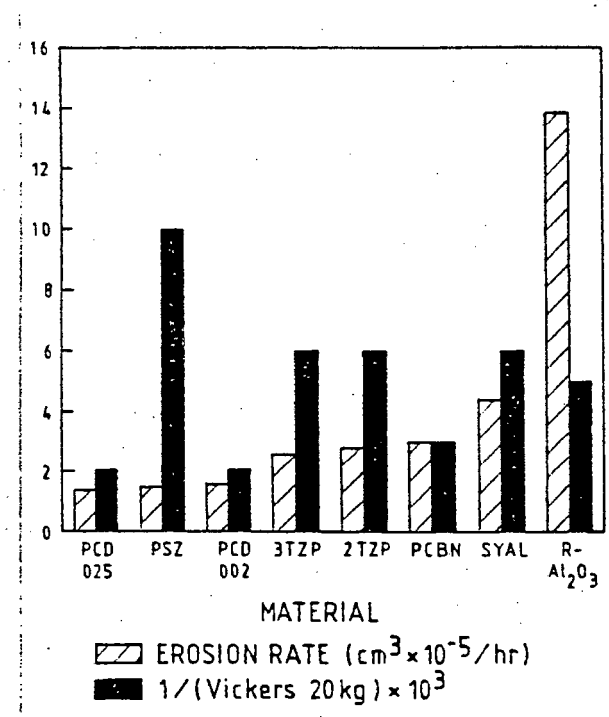

Fig.60 Cavitation erosion rates and normalised inverse hardnesses for the materials under investigation.

Figures 61-65 show property-performance relationships for the materials in cavitation erosion. There is in general far less correlation with any of the properties than for solid particle erosion. A good correlation exists between the grain sizes of the ceramics, and there is a strong correlation between porosity and erosion rate for the alumina materials. The anomalously good performance of the zirconias is even more evident than for solid particle erosion (see above).

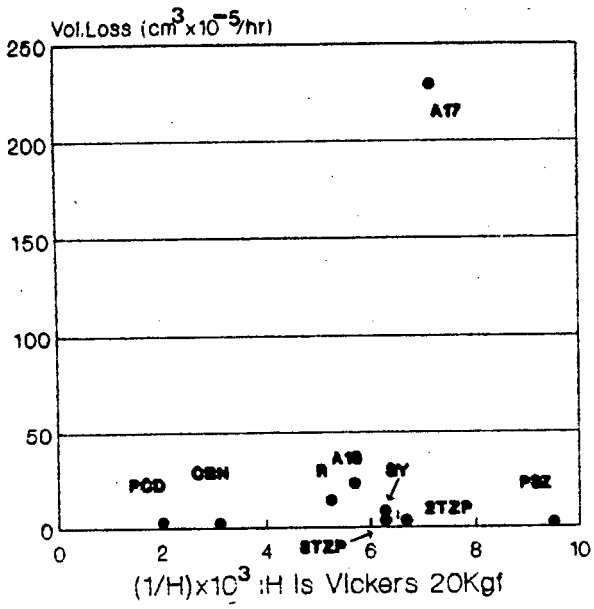

Fig.61 Cavitation erosion versus the inverse of hardness.

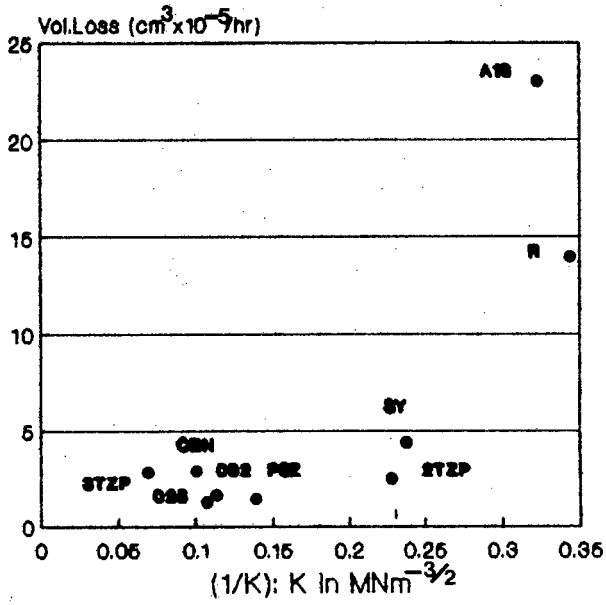

Fig.62 Cavitation erosion versus the inverse of toughness.

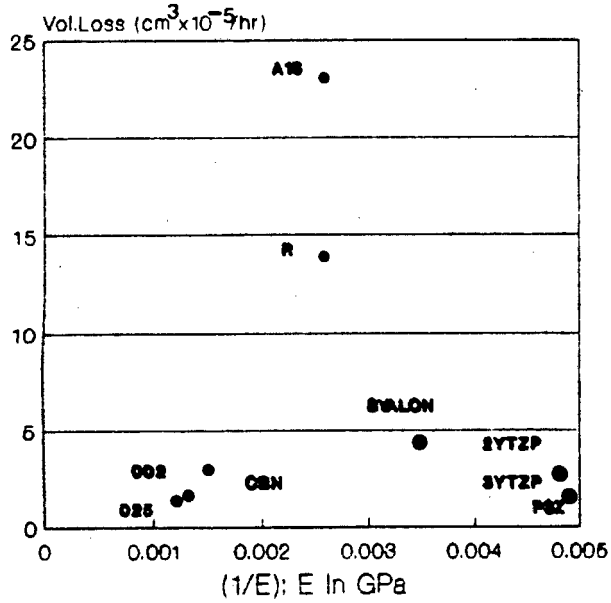

Fig.63 Cavitation erosion rate versus the inverse of Youngs modulus.

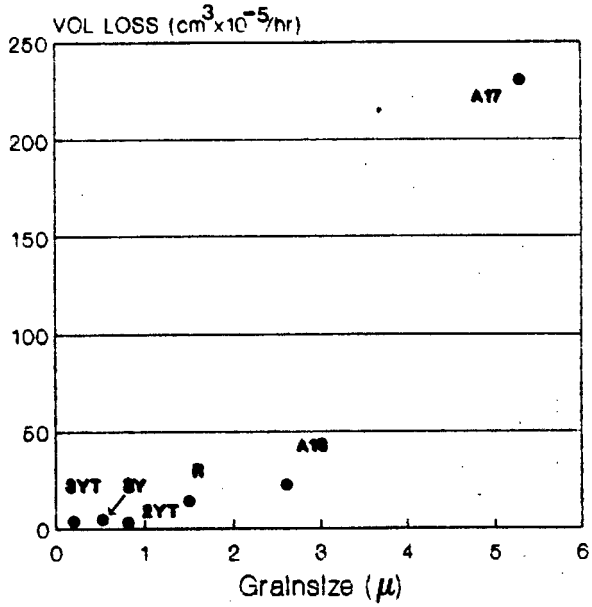

Fig.64 Cavitation erosion versus grain size for the ceramic materials.

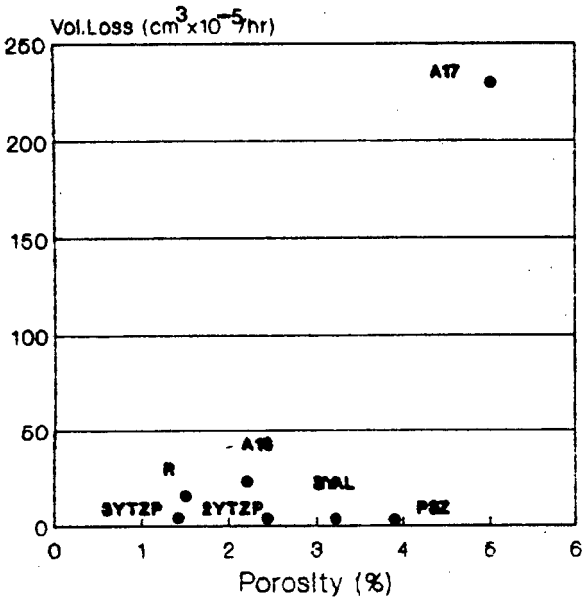

Fig.65 Cavitation erosion rate versus porosity for the ceramic materials. Note the strong correlation for alumina.

5.3.4: X-ray diffraction evaluation of stress induced tetragonal to monoclinic transformation in zirconia.

The amount of tetragonal phase in the as-polished, particle eroded and steady state cavitation erosion (25 hours) zirconias has been evaluated using the formula of Evans, Stevens and Binner[49]. The integrated intensities of the relevant x-ray peaks were determined using planimetry.

The results of the calculations are presented in table 3 and a typical trace is presented for reference in figure 66. The volume fractions of the tetragonal phase (f_t) before and after erosion indicate:

1.) that both cavitation erosion and solid particle erosion induce transformation in 2YTZP.

2.) that negligible transformation takes place in either 3YTZP or PSZ due to cavitation, but that solid particle erosion does induce transformation.

3.) that 2YTZP then is by far the most transformable of the materials, and

4.) that far more transformation is induced by solid particle erosion than cavitation erosion.

It must be noted that the results for the partially stabilised material cannot be directly compared with the results for the TZP materials. The fraction of tetragonal phase calculated for the latter materials is a reasonably accurate volume fraction. In the case of the PSZ however, the major phase is cubic and this has been ignored in the calculation. The figures in table 3 therefore must should be normalised to take into account real tetragonal content in the material. They do however give an indication of the extent to which the tetragonal precipitates within the cubic matrix have transformed.

Material and condition		$I_t(111)$	$I_m(111)$	$I_m(11\bar{1})$	f_t *
PSZ:	polished	1117.4	13.0	35.5	0.96
	SPE	1206.5	-	302.9	0.80
	Cav.	1559.6	2.8	81.7	0.95
2TZP	polished	711.2	-	-	1.00
	SPE	641.16	-	189.9	0.77
	Cav.	600.1	2.9	75.5	0.88
3TZP	polished	737.1	-	-	1.00
	SPE	866.2	-	25.8	0.97
	Cav.	645.6	-	7.7	0.99

* $f_t = \{I_t(111)\}/\{I_t(111)+I_m(111)+I_m(11\bar{1})\}$ (ref.49)
where ft is the volume fraction of the tetragonal phase.

Table 3 Results of X-ray diffraction evaluation of tetragonal phase content before and after erosion.

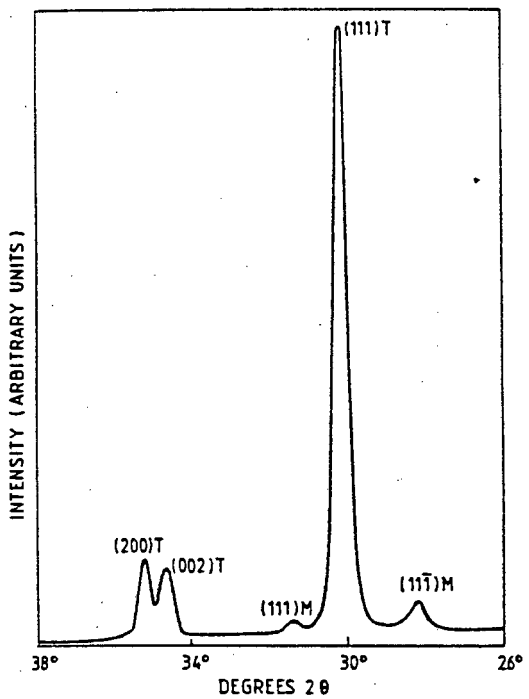

Fig.66 Typical x-ray trace showing the relevant tetragonal and monoclinic peaks for calculation of the tetragonal phase content. The figure here shows the steady state cavitation erosion result for 2YTZP.

CHAPTER 6.

DISCUSSION

6.1: SOLID PARTICLE EROSION.

6.1.1: Individual material responses.

The ceramic materials are treated separately from the ultrahard materials here because the two groups of materials are subjected to different erosion regimes; the hardness of the silicon carbide grit is intermediate between the ultrahard materials and the ceramics, being softer than the former and harder than the latter. This is dealt with in more detail in the comparative section below.

6.1.1.1: Ceramic materials.

6.1.1.1.1: Polycrystalline aluminium oxide.

6.1.1.1.1.1: Single impacts: basic erosion mechanisms.

Single particle impact sites observed are consistent with an elastic-plastic interaction between erosive particle and target material. Almost all impact sites exhibit partly or well developed lateral cracks extending from below the surface of the impact, upward toward the free surface. Where these microcracks are well developed, material removal has taken place in the form of brittle intergranular spallation. This crack morphology is consistent with numerical analyses of Evans[17]. His calculations of the stress distributions during penetration and unloading predicts that lateral cracking will be initiated above a fracture threshhold

provided that an adequate density of crack precursors exists in the vicinity of the plastic zone. In the aluminas here, intergranular porosity serves to concentrate stresses at grain junctions and triple points. The interaction between porosity and microcracking is seen in figure 11. Crack propagation is driven by residual stresses arising fron elastic mismatch at the elastic-plastic boundary and is largely determined by the local effective compliance in this vicinity.

It is important to note that both the plastic (indentation and extrusion) and brittle (microcracking) features observed here are of the same scale as the microstructural features. This goes some way to explaining the partial failure of the fracture mechanical approach to erosive wear since this approach is based on macro-properties. These properties reflect a material's response to stress fields which are different to those responsible for microplasticity and microcracking. Consequently any powerful predictive treatment of erosion must be based on parameters which are analysed on the microscale. This will include intrinsic structural properties due to bonding and crystal structure (intrinsic dynamic hardness and toughness, thermal properties etc.) and will also include microstructural features (grain size, morphology) and defect structures (porosity, impurities etc.) The effect of porosity as a stress concentrator has been discussed above while the intergranular spallation is a direct manifestation of the interaction between the microstructure itself and the imposed stress field. It is apparent from almost all of the micrographs of the solid particle erosion of ceramics which have a grain size smaller or comparable to the scale of the indentation, that fracture is almost entirely intergranular. This is indicative of the inherent weaknesses of grain boundaries in ceramics. Non-close packing between the directionally bonded atoms at the crystallite boundaries

results in severe weakness. This situation is aggravated by stress concentration by angular intergranular porosity, especially in the alumina materials.

Wiederhorn and Hockey[16] have pointed out the importance of plasticity in the erosion of ceramics and ascribe the relative extents of plasticity and fracture to differences in bonding. This must indeed be the case and it will be argued here that a scale effect due to the relative size of microstucture to impact effect will strongly perturb the effects of bonding. The differences are not at first altogether clear from observations of single impact sites, but are clear in the steady state and are discussed in more detail below.

6.1.1.1.1.2: Steady state erosion.

In the past it has generally been assumed that each single impact event contributes individually to erosion. This approach assumes that lateral cracks link up below the surface of the material and result in material removal. This idea has been revised in the light of subsequent work and consequent work on metals. It is now realised that more than one impact may be required to remove material and that the number of impacts required to remove a given volume of target may be thought of as an index of the materials' resistance to erosion. In general this idea has not received the attention it deserves.

Observations of the steady state erosion surfaces in this investigation show that the steady state itself exhibits both plastic features and brittle spallation of material. There is in all cases evidence for compaction of previously deformed material so that the ceramic's ability to accumulate residual damage contributes to its erosive performance. The importance of work hardenability to good

wear resistance has been emphasised by Ball[50]. It is clear moreover that the extent of plasticity relative to fracture is a fairly sensitive function of grain size where the grains are close in size to the impact event.

As the grain size decreases the extent of plasticity relative to fracture increases (see figures 8, 10 and 12) as does the material's effective capacity for residual (subcritical) damage. This manifests itself in the superior performances of the finer grain sizes of material. Figure 37 shows that a good correlation exists between the grain size and the normalised volume loss. The above statement must be qualified: the grain size of a ceramic is not in general an independent parameter, but is interrelated with porosity and impurity segregation. Consequently, the variation of many properties including microhardness and microtoughness may not be ascribed to a variation in any of three parameters above alone. Indeed in the aluminas here, the porosity increases almost linearly with grain size.

Now the increasing microhardness with decreasing grain size indicates a decreasing capacity for flow with decreasing grain size. This represents an apparent anomaly, but it must be noted that the decrease in hardness with increasing grain size must at least in part be ascribed to the effect of porosity since the size of the pores represents a significant fraction of a microhardness indentation. In addition, microhardness tests in alumina caused both microplasticity and microcracking here, so that the hardness value should be taken as representative of resistance to both.

It is thought that the grain size effects in the erosion tests here are largely due to effects of anisotropy in the non-cubic alumina. These effects of the anisotropy exhibit a functional dependance on grainsize. In polycrystalline

materials under load, elastic differences across grain boundaries due to different orientations in adjacent grains result in an increase or decrease of the applied stress. This stress is superimposed on stresses at grain boundaries which result from cooling after manufacture, due to thermal anisotropy. The latter effect is the larger of the two. The nett result is a significant magnification of the applied stress at those grain boundaries which experience constructive superposition.

If this stress exceeds the threshold energy for either grain boundary or transgranular fracture, then microcracking will occur. That this result is a function of grain size may be understood by consideration of the requirement for microcracking: that the volume source and surface sink of strain energy be equated. This leads naturally to a critical condition for grain size below which microcracking becomes increasingly less probable[51].

6.1.1.1.1.3: Thermomechanical effects during erosion of alumina.

Features have been observed at some impact sites in alumina which suggest that melting has taken place. Examples are shown in figures 29-30 where teardrop shaped features, elongated stringers and droplets of material may be seen. Because severe thermomechanical effects are expected at the high strain rates experienced during solid particle erosion it is of interest and import to ascertain the mechanisms and extent of the heat generation and melting features. This will yield information on the effect of thermomechanical heating on erosion itself.

The morphology of the features in figures 29 and 30 suggest that the melting is a surface phenemenon. Yust and Crouse[28] assumed that the melting features they observed in

polycrystalline alumina and mullite were analogous to the base of a shear lip of an impact site in a metal where adiabatic shear has been observed to occur . In this study however, droplets were observed in impact sites where no well formed shear lips were present (fig 30). It is therefore suggested that the approach must assume that the catastrophic thermoplastic shear is taking place at the interface between the particle and target and not in the bulk of the material. This surface is subjected to high shear stresses due both to the friction and high transient stress pulse during impact. It is of interest that the application of Yust and Crouse's approach to the problem using the experimental details appropriate to the tests here, nevertheless yields a temperature in excess of the melting temperature of alumina.

It would seem an attractive proposition to examine the energetic considerations and determine whether heating a typical shear zone would consume a significant fraction of the energy provided by the momentum of the impacting particle. The minimal utility of a quantitative energetic calculation has been pointed out by Evans[17]; a large unquantifiable amount of energy is dissipated at the boundaries by elastic waves during the elastic plastic impact. Nevertheless, a conservative order of magnitude calculation of the ratio of the kinetic energy of an impinging particle to the amount of energy required to melt the small highly sheared region of a typical impact site indicates that the latter may constitute a few percent of the former. It is not clear , bearing in mind the numerous mechanisms absorbing energy, whether this would be sufficient for thermal effects to play any significant role.

If local heating raises the temperature of the material to a large fraction of its melting point, then one will expect the flow stress to be reduced. The increase in temperature

will increase the possibility of dislocation formation and growth and will also reduce the Peierls-Nabarro stress. Moreover thermal expansion will take place and this may be thought of as representing a lateral crack driving force.
It was at first thought that the melting features were composed of alumina. It has however been suggested[52] that, since the silicon carbide particles have a coherent oxide layer on their surfaces, the extrusion and melting of such a layer of silica would be more probable due to its lower melting point and lower shear stress.

Furthermore, concomitant diffusion at the high temperatures would result in the formation of a low temperature (about 1500 degrees centigrade) eutectoid product in the Al_2O_3-SiO_2 system. This may be seen from the phase diagram below in figure 67.

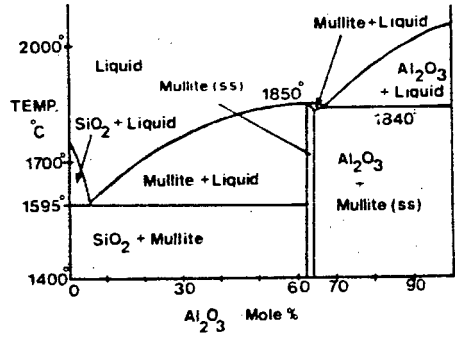

Figure 67 The alumina-silica binary system showing a eutectic at 1595 degrees centigrade and about 5 mole per cent alumina.

If the precise composition of the melting features could be ascertained, then an idea of the thermal history required to form such features could be induced from the dynamic phase diagram. EDS work suggests that there is a 0.87-5.92 per cent silicon content in the features. Unfortunately this value cannot be regarded as being quantitatively accurate since the silicon and aluminium peaks are at a low energy and overlap. More importantly, the x-ray sampling and yield areas are much larger than the features themselves. This would require delicate TEM replica work or advanced techniques such as secondary ion mass spectroscopy.

A simple theoretical approach to the problem has been taken and it will be seen that whether the melting features are entirely alumina or entirely silica, it is relatively easy to show theoretically that temperatures in excess of the melting temperatures may be reached provided that certain assumptions are accepted.

Hutchings and Levy[53] have presented an approach for the estimation of the maximum temperature rise at an impact site in metals. This approach may be extended to erosion of alumina provided that certain of his assumptions may be validly extended to the conditions here. This will be shown to be the case.

We assume:

1) that perfectly adiabatic conditions prevail. It will be shown below that this is not entirely true, but that the conditions used in the study here lie close to the adiabatic/isothermal boundary. It will be seen however that the calculation below yields a temperature well in excess of the melting temperature of alumina, so that it might be expected that the melting temperature will still be reached in the absence of entirely adiabatic conditions.

2) all the kinetic energy of the particle goes into the the volume of material that is plastically deformed. Many of the smaller impact sites are entirely plastic so that little energy goes into fracture. Some of the initial kinetic energy will of course be translated into energy of recoil.

3) the plastic volume above is equal to the indentation volume. This last assumption is not strictly valid but is conservative.

Now using the approach in Hutchings and Levy[53], a simple formula for the temperature reached is given by:

$T_{max}=P_r/\rho C_p$

T: temperature

P_r: pressure exerted by particle (assumed equal to quasi-static indentation hardness)

C_p: specific heat

ρ: density of deforming material.

For alumina, P_r=18.6 GPa, C_p=1040 J/kgK and ρ=3980 kg/m3, and T_{max} is calculated as 4490 K. Similarly for silica, P_r =5.0, C_p=750 and ρ=2200 so that Tmax equals 3030 K.

Note that if

a) the load is higher than assumed (reasonable due to the dynamic conditions here) or

b) the energy is released into a smaller volume than assumed (reasonable if plastic instability occurs)

then the calculated temperatures will be higher. On the other hand the assumption that all the initial kinetic energy goes into plastic flow is often incorrect here.

An alternative approach may be adopted. Following the

approach of Nabarro[54] where flow is localised in a region of width (2B), cross sectional area (A), and elongates by (e) under a load (P), the work done on the region will be (P.e). Assuming that most of the work is converted into heat under close to adiabatic conditions, the rise in temperature will be:

$$T = Pe/2AB\rho C_p \qquad \text{so that}$$

$Pe/2AB$ equates with P_r above.

In this case, one can calculate the approximate average force exerted by the particle on the target from the equations of motion. Then assuming alternately that the alumina or the silica is extruded under these conditions and estimating the geometry of the material that goes plastically unstable from SEM observations one may now calculate the flash temperature.

using $P=0.4$ (N)

$A=10^{-7}$(m)

$B=5*10^{-6}$(m)

$\rho=3520$ (Al_2O_3) and 3100 (SiO_2) (kg/m^3)

and $C_p=1040$ (Al_2O_3) and 750 (SiO_2) (J/kgK)

then a 2 percent elongation in the alumina will generate a flash temperature of 2200 K while 3400 K will be generated in the silica.

The assumption above of perfectly adiabatic conditions will pertain if the rate of generation of heat exceeds the deformation rate. This is analogous to the question of whether the conduction of heat away from the site of generation proceeds faster than the movement of the elastic plastic boundary into the target material.

The treatment of Hutchings and Levy[53] may again be extended to the conditions used here to consider whether adiabatic conditions prevail.

Assumptions:

1) If the depth of the plastic zone associated with impact (x_p) exceeds the root mean square thermal diffusion distance from the impact site (x_d) then adiabatic conditions will prevail. Isothermal conditions will prevail in the opposite case.

2) The expression for x_p below assumes perfectly plastic impact in its derivation. Melting has been observed at impact sites in alumina in this study where interaction was entirely plastic, so that this expression is assumed to be valid for at least some of the impacts.

Now $x_p = rv(2\rho_p/3P_r)^{0.5}$ Hutchings[55]

and $x_d = (6Kt)^{0.5}$ where t is the impact time

and $t = (\pi/2)r(2\rho_p/3P_r)^{0.5}$ Tabor[56]

then $x_p/x_d = v(r/3\pi K)^{0.5}(2\rho_p/3P_r)^{0.25}$ Hutchings and Levy[53]

where K: thermal diffusivity ($K = k/\rho C_p$)
r: particle radius
ρ_p: particle density
P_r: pressure
v: particle velocity

Assuming again that P= 18.6 GPa (the quasi-static hardness of the alumina), ρ_p=3300 (kg/m^3), and published values of K lie between $2.03*10^{-6}$ and $1.94*10^{-5}$ (m^2/s). One may now construct a plot of particle size versus velocity which delineates the boundary between adiabatic and isothermal conditions ($x_p = x_d$). This plot is shown in figure 68 and the results for Hutchings and Levy[53] for steel are included for comparison. The conditions used for the erosion of alumina here may lie either within the adiabatic or isothermal regimes, depending on the true value of K.

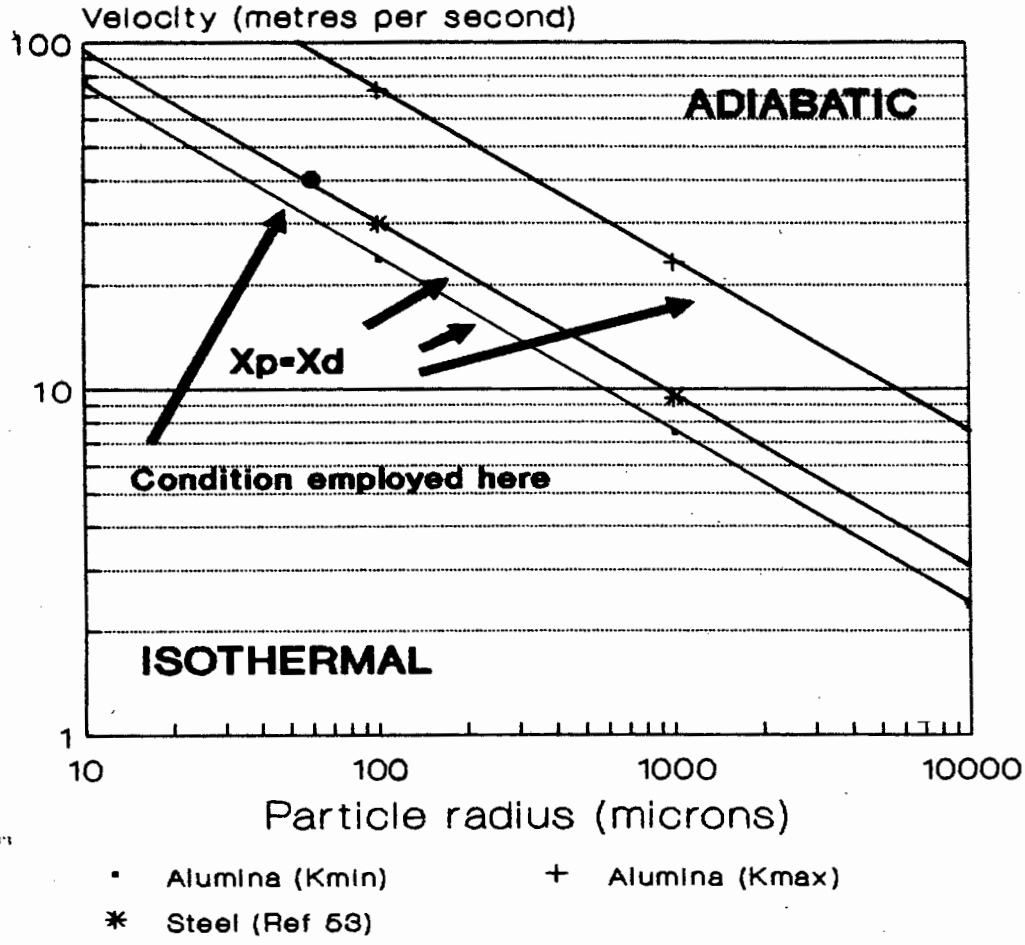

Fig. 68 Particle size versus velocity delineating the adiabatic-isothermal boundary for particle erosion.

Although highly adiabatic conditions might have been expected to pertain in the ceramics, the effect of the lower conductivity is clearly greatly offset by the much higher pressures at the impact sites. This serves to enhance the movement of the plastic boundary, but has little effect of the thermal flow. The calculations above, of the mean temperature that may be generated indicate that extremely high temperatures will be reached under fully adiabatic conditions. It seems reasonable therefore to assume that reasonably high temperatures will be generated even under close to adiabatic conditions.

If one accepts then that significant temperatures are generated at impact sites in alumina under close to adiabatic conditions it is a natural consequence to evaluate whether any thermal reinforcement takes place.

We seek to compare the distance through which heat diffuses in the interval between impact on the same site with the dimensions of the impact site or the depth of the plastic zone. The former length (X_i) is determined by the root mean square diffusion distance and the time between impacts.

Now $X_i = (Kt)^{0.5}$ where t is the time between impacts

i.e. $t = \pi r^3 \rho_p d^2 / 3a^2 m$ (see Levy and Hutchings)[53], so that

$$X_i/a = (\pi K d^2 P_r / 8 m r v^2)^{0.5}$$

where m: the particle feed rate.

d: chordal diameter of eroded area

a: chordal radius of indentation.

Then one can construct a plot of X_i/a versus the feed rate. (figure 69). For steels[53], at the maximum practical feed rate for these conditions (0.1g/s) the ratio of X_i to a is about three hundred. That is to say that heat generated during impact diffuses more than a hundred times the characteristic dimensions of an impact during the time of that impact. This implies that superpositional effects must be negligible. For alumina, the ratio of X_i to a is even greater and reinforcement will be less likely than for steel.

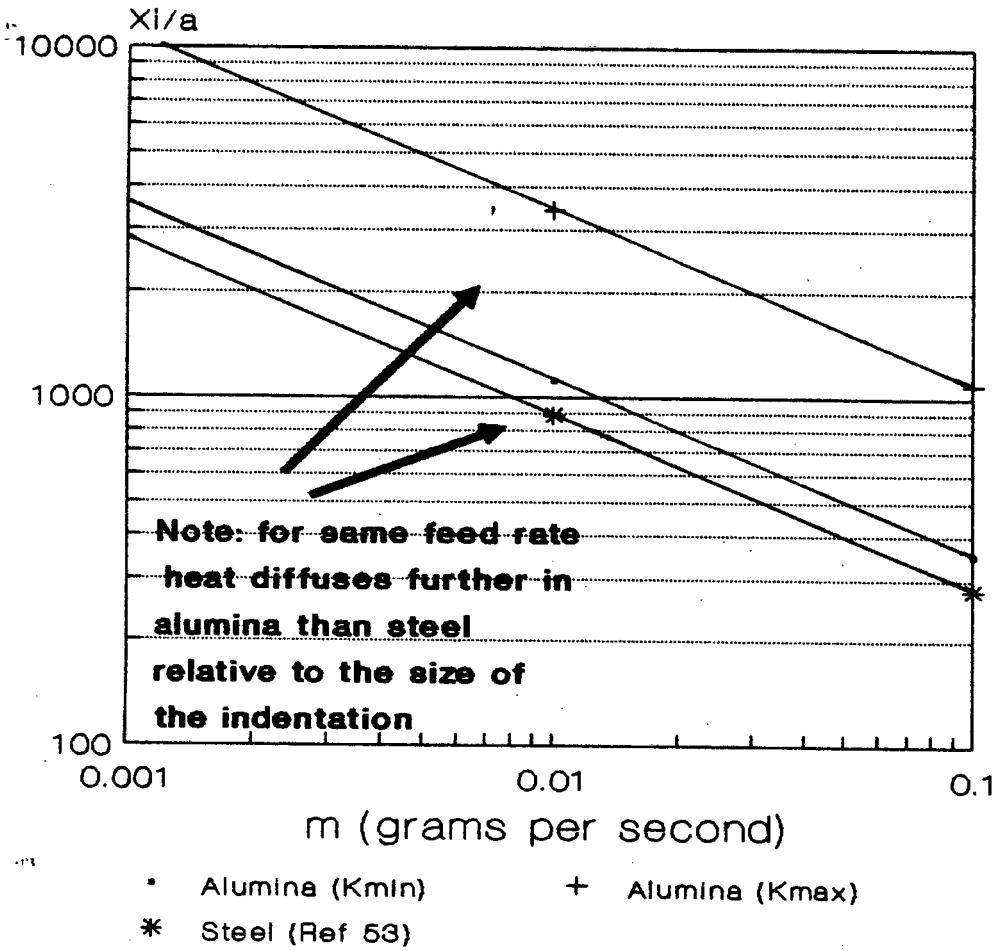

Fig.69 Plot of x_i/a versus the feed rate (m) from which the extent of thermal reinforcement may be deduced.

The above calculations and considerations do in general support the observations of melting at particle impact sites, although it is not yet clear whether the melting features are alumina, silica or a binary mixture of the two. Thermal reinforcement seems highly unlikely and it is uncertain whether these thermal effects play any significant role in the magnitude of the erosion of these materials. The largest difficulty in the solution of this problem is the deconvolution of thermal, mechanical and microstructural effects. This will have to be the aim of further research in this field.

6.1.1.1.2: Sialon.

6.1.1.1.2.1: Single impacts : basic erosion mechanisms.

Sialon consists of a fine phase mixture. The details of single impacts are similar to the aluminas however with typical elastic-plastic interaction exhibited. Lateral venting is less severe and more plasticity is evident. This observation is consistent with the higher toughness and lower hardness of the sialon. It is thought that the glassy second phase (YAG) provided some degree of accomodation for stresses during impact. A second phase dispersed in a ceramic matrix increases the resistance to crack propagation provided the second phase has a higher critical energy dissipation rate than the matrix[57]. It would appear that the glassy phase in this material acts in a positive manner since intergranular fracture appears predominately at boundaries where there is less glassy phase.

The low porosity prevents stress magnification and inhibits well formed microcracks while the fine grain size results in an effectively polycrystalline toughness response at the impact site and this will be higher than the single crystal value. In addition, the relatively high aspect ratio of the crystallites provides an interlocking type of microstructure which makes material removal more difficult. This observation has also been made for silicon nitride by Wada and Watanabe[58].

6.1.1.1.2.2: Steady state erosion.

Plastic flow, compaction, platelet formation and subsequent spallation are evident during the steady state erosion of sialon. The material exhibits good ability for absorbing energy without any mass loss. Several concentric or adjacent

impacts are apparently necessary to form and chip off a platelet.

6.1.1.1.3: Zirconia:

6.1.1.1.3.1: Single impacts: basic erosion mechanisms.

Single impacts in both TZP materials are similar to the other ceramics, showing residual plastic indentation accompanied by intergranular lateral venting. This is not entirely true for PSZ where the grain size is much greater than the size of each impact event. In this latter case, the relative extents of plasticity and fracture are quite dependant on the orientation of the impacted grain with respect to the imposed stress system. Lateral cracking here proceeds most often in a transgranular conchoidal manner.

6.1.1.1.3.2: Steady state erosion

Steady state erosion surfaces of the TZP materials are extremely similar in morphology to that of sialon. A greater amount of plastic compaction and extrusion is evident however. Although the PSZ also shows significant plasticity, there is a significant amount of brittle transgranular conchoidal fracture.

6.1.1.1.3.3: The effect of transformation on erosion response.

Close examination of the areas around single impacts on both TZP materials shows that the deformation causes a slight rumpling of the polished surfaces. This is characteristic of the t-m transformation in the material and results from the deviatoric and dilatational components of the martensitic transformation. X-ray diffraction traces indicate that extensive transformation has taken place from the tetragonal

to the monoclinic phase.

This is expected to influence erosion: Plasticity should be enhanced by the transformation (TRIP) and the transformation itself should act as an energy absorbing mechanism. The volume expansion (3-5%) associated with the phenomenon will serve to set up compressive biaxial stresses on the surface of the ceramic, and these will both raise the effective hardness and toughness at the surface and will inhibit venting by lateral cracks. This will be most effective provided that the surface remains relatively flat. Unconstrained material that is suitably oriented will be encouraged to spall off the surface by the transformation with its associated dilatational and deviatoric changes.

It is conjectured that this is part of the reason that the 2YTZP (which is more transformable) performs slightly worse than the 3YTZP in steady state erosion. In addition, the 2YTZP material is slightly softer than the 3YTZP. It is not however certain how accurate the hardness tests are because transformation will be responsible for accommodation that might otherwise have gone entirely into plastic flow[58].

6.1.1.2: Superhard materials.

6.1.1.2.1: Cubic boron nitride.

Although it was found impossible to distinguish single impacts on the as received surface from the surface itself, the morphology of the steady state surface gave information on the mechanisms of damage. Compaction and extrusion of the AlB_2 binder bhase occurs. Sufficient erosion of this phase results in increasing exposure of the CBN grains which are ultimately knocked off the surface.

No damage to the grains themselves could be identified and this is consistent with the superior hardness of CBN to the SiC erodent and also with the accommodating and cushioning role of the softer second phase.

6.1.1.2.2: Polycrystalline diamond.

In contrast to PCBN, the diamond compacts should be considered as having a scaffold [59] or skeletal type structure which results from the intergrowth of the grains. The result is that extrusion of the second phase does not occur because no relative motion of diamond grains is possible. The small volume losses measured result from the impact of sharp corners on exposed cobalt. This would explain the slightly higher wear rate in PCD025 since the coarser structure in this material results in exposure of larger areas of free cobalt. In the fine 002 grade, many of the cobalt pools are well below the typical effective radius of curvature of the impacting particles and are consequently inaccessible.In general it appears as if the stresses resulting from impact are both insufficient to damage the diamond crystallites and insufficient to break the intergrown regions betweeen the original grains.

6.1.2: Comparisons between materials.

Figure 32 presents the results of all the materials tested as a function of the mass of erodent impinged upon them. Cubic boron nitride is the only material that shows any sign of incubation. This seems logical because of the observed plastic flow of the binder phase. Further, the mode of erosion is extreme for the ceramics, and close to harmless for the diamond materials and these are thus not expected to show significant incubation. In the case of the diamond, the materials are in a non-erosive regime due to their superior hardness, whilst the ceramics erode so fast that any

incubation is swamped. Srinivasan and Scattergood[60] have also found similar effects arising from the ratio of particle to target hardness.

The vastly superior performances of the superhard materials is a manifestation of their greater hardness than the erosive grit as well as good micro-toughness. Within the ceramics tested, it is obvious that a fine grain size and low porosity results in good micro-toughness and is beneficial. Optimisation of these parameters reduces the extent of fracture per impact event. Since fracture controls material removal and strength degradation, it effectively controls the severity of the damage.

It should be noted from figure 35 that the indentation fracture toughness values correlate inversely with their performances. Since it does not seem physically sensible to ascribe high erosion rates with high toughnesses, it must be assumed that toughness values themselves are either incorrect or evaluated at an inappropriate scale or strain rate. Where the details of an indentation are close in scale to the microstructure of a polycrystalline ceramic, interaction between the two will occur this and can convolute the evolution of radial cracks at the indentation corners. In the extreme case as in A17, spallation of whole grains of the material can act as an alternative energy absorption mechanism so that the length of the cracks formed does not accurately reflect the fracture toughness, but a higher value. Moreover where the radial cracks themselves are intergranular and change direction often, it is difficult to measure their real length with precision using a graticule.

Although the zirconia samples perform similarly to the other ceramics, figures 34-37 show that they exhibit anomalous property-performance relationships. Better performance is

displayed than would intuitively be expected from their hardnesses and this must be attributed to the activation of the stress induced transformation.

6.2: CAVITATION EROSION.

6.2.1: Individual material responses.

6.2.1.1: Alumina.

6.2.1.1.1: Initiation and basic mechanisms of damage.

There is no evidence in the SEM micrographs (figs.39-44) of any plastic deformation in alumina. It is expected that transmission electron microscopy should show otherwise on the basis of the work by Miyoshi et al[36] but plastic deformation is clearly not a dominant or significant mechanism here. The transient stresses caused by cavity collapse are magnified and concentrated at grain boundaries and porosities in particular. This is clearly shown in figures 39 and 41. The anisotropy in the materials is expected to play a role for the strain energy considerations discussed for alumina under solid particle erosion above. This will also account to some extent for the similar grainsize- and porosity-volume loss relationships shown in figures 64 and 65.

Microcracking initiated at grain boundaries grows subcritically until grains which are not well constrained by their neighbours spall off the surface. Little or no evidence of transgranular fracture was seen.

6.2.1.1.2: Steady state.

Removal of single grains of the material by microcracking of the apparently extremely weak grain boundaries soon results in the formation of pits in the surface of the material. These spread until the whole surface is damaged. Propagation is easier than nucleation for two reasons: grains at the edge of a pit are not biaxially constrained and are easier to remove than than grains surrounded by a flat polished surface.

The pits themselves also serve both as initiation sites for cavity nucleation and also channel both the stress pulses and liquid microjets that result from cavity collapse. It would be expected that this manifests itself in a significant incubation period. The aluminas however cavitate fast and reach steady state in a fraction of the time of each test cycle (1 hour) and thus this is not evident.

6.2.1.2: Sialon.

6.2.1.2.1: Initiation and basic mechanisms.

Damage in sialon initiates at porosity where grains begin to spall of the edges of the large (larger in general than the grain size) pores. On the polished surface of the sample, the glassy second phase is preferentially removed, but there is no evidence for the evolution of microcracking. It is postulated that the fine, tough structure requires a large amount of energy to remove an individual grain of material, both due to the presence of the glassy phase and due to the good interlocking of crystallites afforded by their high aspect ratios.

6.2.1.2.2: Steady state.

The steady state surface in figure 46 shows that erosion proceeds in an entirely intergranular manner. The grains interlock to a moderate degree and the good bonding between the fine crystallites is manifested in the rough topography of the erosion surface.

6.2.1.3: Zirconia.

6.2.1.3.1: Partially stabilised zirconia.

6.2.1.3.1.1: Initiation and basic mechanisms.

Damage initiates at inter- and intragranular porosity. The former is the dominant site. Extrinsic flaws on the polished surface of the PSZ are also responsible for damage initiation and propagation. The effect of a scratch on a damage site is clearly shown in figure 70 below.

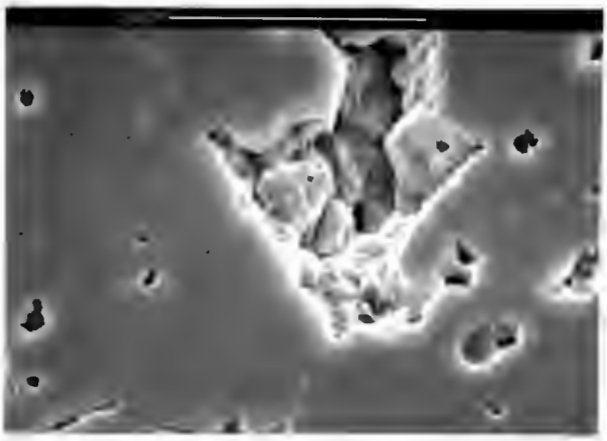

Fig.70. Initiation of cavitation damage at a scratch on the surface of PSZ.

There are three possible reasons for this. Firstly, the scratch may effect the nucleation of, and geometry of collapse of cavities themselves. Further, the scratch will serve to concentrate stresses induced by the collapse. Finally, residual compressive stresses are present below the scratch itself due to plastic deformation. Encroachment of a damaged region (pit) upon such a region will remove the constraint upon the region whereupon the compressive stresses will be released in the direction in which the constraint has been removed. This can be expected to result in enhanced material removal in this area.

Damage initiates at grain boundaries and proceeds in an almost entirely transgranular manner. In some cases, the polishing leaves only small sections of grains exposed to the surface. The spallation of one such grain is shown in figure 71 below.

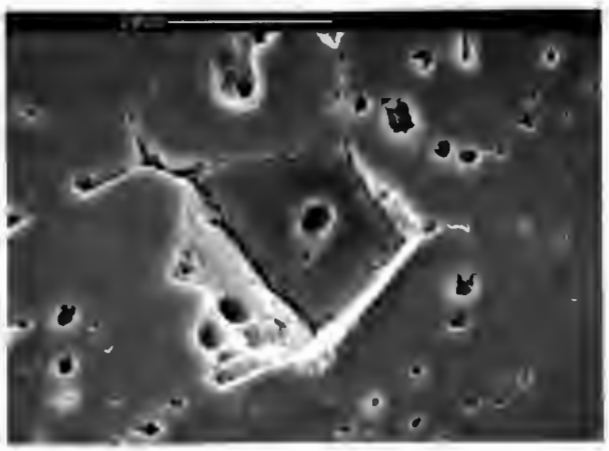

Fig.71: Spallation of small section of grain left at surface due to polishing.

6.2.1.3.1.2 Steady state.

Once the steady state has been reached, erosion progresses by gradual transgranular attrition. There is no evidence from the SEM micrographs of any transformation of the tetragonal precipitates. It is postulated therefore that the the slow rate of material removal is due both to the toughness of the material and its large grain size which is thought to be greater than the size of individual cavitation events. This latter factor prevents wholesale intergranular spallation.

6.2.1.3.2: Tetragonal zirconia polycrystal.

6.2.1.3.2.1: Initiation and basic mechanisms of damage.

Both the TZP materials perform similarly in nature. Intergranular microcracking is apparent during the incubation stage of erosion, and this cracking is intimately related to the porosity distribution.

6.2.1.3.2.2: Steady state.

The steady state morphology of both 2- and 3YTZP is entirely intergranular. The macroscopic morphologies of the erosion surfaces are slightly different and it is thought that this is a grain size effect.

6.2.1.2.2.3: Transformation effects.

There is no obvious evidence of transformation either in the initiation of steady state surfaces of 2 or 3YTZP. XRD traces indicate that some amount of transformation does indeed take place however. This would result in spallation of suitably oriented and exposed single grains of material

as seen in figures 49 and 51. Any transformation taking place is expected to to assist erosion resistance both by absorption of energy through the transformation itself, and because of the effectively greater hardness of the daughter phase than the parent. It is possible that the small amounts of transformation measured indicate that the transformation is reversible and this would act as a dynamic erosion resistant mechanism without rapid accumulation of damage. This question will have to be the question of more specific future work.

The results here suggest that an optimum index of transformability exists for superior erosion resistance. The 2Y% material is more transformable than the 3% material and it performs better than the other material during incubation, but worse during the steady state. This may be understood by consideration of the surface topography. During incubation, where the surface is polished, transformation in grains close to the surface of the material will result in compressive stresses in the surface layer and these should assist resistance to erosion. When steady state has been reached however, there is no longer significant constraint on grains near the surface of the material. Thus the transformation and and concomitant volume expansion may begin to assist spallation and is no longer as beneficial. The more transformable material does not therefore perform as well in the steady state.

It is nevertheless clear from the general erosion results that both fully stabilised materialsperform well relative to the other ceramic materials. This is due both to the effect of transformation induced plasticity and the high density of the material which translates moderate mass losses into small volume losses. The latter is of course the more important material design parameter.

6.2.1.4: Cubic boron nitride.

6.2.1.4.1: Initiation and basic damage mechanisms.

Initiation of damage starts in PCBN as the layer of smeared binder (AlB_2) on the surface of the sample is removed. Erosion of the bulk material then begins as the binder between the CBN grains is work-hardened and spalls away, or is extruded between the grains.

6.2.1.4.2: Steady state erosion.

Once a significant amount of AlB_2 has been removed, there is no longer sufficient support for the CBN grains, and these spall off the surface. This leaves exposed binder underneath which then erodes quickly again to expose the hard ceramic grains. The incubation exhibited is a result of the absorption of energy by the binder on the surface of the as-ground surface, and the binder between the grains of the material. The binder in this latter region is more constrained than the exposed binder in the steady state and consequently more resistant to removal by the cyclic stresses.

6.2.1.5: Polycrystalline diamond.

6.2.1.5.1: Initiation and basic damage mechanisms.

Damage begins in a similar manner to the CBN. Free cobalt smeared on the surface of the PCD is removed after which the intergranular cobalt is attacked. The high initial erosion rate and inverse type of incubation seems to indicate that the preparation techniques either leave larger amounts of free cobalt on the surface or cause damage to the surface layers resulting in easy removal by cavitation erosion.

6.2.1.5.2: Steady state.

As the mechanism of attack changes from erosion of exposed cobalt to attack of the rigid diamond skeleton, the erosion rate drops remarkably. Where intergrowth of diamond grains has not been entirely succesful, only small necks join the grains, and the radii of curvature of these necks can be quite high. Such areas are vulnerable to the cavitation stresses which have been concentrated by the angular areas from which cobalt has been removed. Isolated fracture occurs and this results in a small but finite mass loss. It is again postulated that the slightly lower erosion rate of PCD025 is due to its larger grain size relative to the cavitation events.

6.2.1.6: Comparisons between materials.

In the ceramic, the very brittle, angular grained aluminas perform the worse in cavitation. The fine grained zirconias and the sialon perform much better, while the coarse grained PSZ performs remarkably well. The good resistance of the PSZ may be understood on the basis of the work of Miyoshi et al[36] comparing the resistance of single and polycrystalline silicon carbide. These workers found that the resistance of the single crystal was higher than the polycrystalline material. The grain size of the PSZ is large and it seems likely that each cavitation event effectively samples a single crystal.Of the ultrahard materials, the PCD materials perform in a similar manner, while the performance of the PCBN is disappointingly high.

The micrographs of cavitation erosion of ceramics indicate extreme sensitivity to microstructure and perfection. This includes grain size, angularity, and porosity size and distribution and is reflected in figures 62, 64 and 65, which show that cavitation is in general sensitive to

toughness and porosity in ceramics. The same sensitivity is not however shown to hardness. This may be expected, since there is no gross deformation apparent in any of the materials tested except for the damage to the ductile binders in the ultrahard materials. Where the matrix is insensitive to the removal of the binder in PCD, good performance results. On the other hand, the CBN erodes quite fast. It is expected that changes in the binder content and grain size could be used to improve the performance of this material.

It is further thought that a size effect exists in the cavitation of these hard materials. The performance of the PSZ must be considered anomalous unless one examines the mode of material removal. The material does not have the best mechanical properties and XRD shows that negligible transformation occurs during erosion. It is the only material that erodes in a predominately transgranular manner and it is thought that this is the result of the grain size significantly exceeding the scale of the erosion events.

The good performance of the TZP is considered to be related to the stress induced transformation and to the fine tough structure. The effect is most marked during incubation.

CHAPTER 7.

SUMMARY AND CONCLUSIONS.

The different natures of cavitation and solid particle erosion lead to the expectation of different material responses to the erosive attack. The results presented indicate that this is indeed the case and the following conclusions may be drawn:

1.) solid particle erosion is controlled by dynamic hardness and microtoughness
2.) fine grained materials with high aspect ratios, low porosity and angularity of crystallites and strong grain boundaries may be expected to perform well where the erodent has a higher hardness than the target.
3.) the presence of glassy intergranular phases and of stress induced transformation will further assist in the accommodation of impact energy and the moderation of erosion.
4.) where it is conceivably possible however, the overwhelming conclusion from this study indicates that superior erosion resistance requires a harder target than the erodent itself.

5.) cavitation erosion in contrast is not as sensitive to hardness and the ultrahard materials' performance does not reflect their much greater hardness. The superior performance of the PCD derives rather from microstructural considerations (i.e. intergrowth between crystallites). In the PCBN where no intergrowth occurs, extrusion of the binder degrades the mechanical properties and leads to moderate erosion rates.
6.) cavitation erosion is extremely sensitive to stress concentating defects including porosity and scratches.

This effect is more pronounced for the ceramic materials where angular grains and porosity must be avoided where possible.

7.) fine grained materials with small amounts of glassy phase appear to perform well, but the use of ceramics with very large grain sizes may result in a single crystal and consequently more resistant response to the cavitation stresses.

8.) accumulation of sub-critical damage is important, where work-hardening of a binder phase or a (preferably reversible) transformation is able to absorb energy that would otherwise be dissipated in the initiation or propagation of microcracking. Strong, skeletal structures like polycrystalline diamond or transformable tough ceramics like zirconia are able then to offer the best resistance under cavitative conditions.

REFERENCES:

1.) Barletta,A., and Ball,A., JCM, 4(1), (1984) 421.

2.) Heathcock,C.J., Protheroe,B.E., and Ball,A., Proc.5th Int.Conf. on Strength of Metals and Alloys, Aachen, West Germany, (1979) 219.

3.) Knapp,R.T., Daly,J.W., and Hammitt,F.G., "Cavitation" McGraw-Hill, New York, (1970).

4.) Engel,P.A., "Impact Wear of Materials", Tribology Series 2, Elsevier, (1978) 104.

5.) Karimi,A., and Martin,J.L., Int.Metals Reviews, Vol.13., (1986) 1.

6.) Sheldon,G.L., and Finnie,I., Trans.ASME 88B (1966) 387.

7.) Hockey,B.J., and Wiederhorn,S.M., Proc. 5th Int. Conf. on Erosion by Solid and Liquid Impact, Cavendish Laboratory, Univ. of Cambridge (1979) 26-1.

8.) Uetz,H., and Fohl,J., Wear, 20 (1972) 299.

9.) Johnson,K.L., "Contact Mechanics", Cambridge University Press, Cambridge, (1985)

10.) Evans,A.G., and Gulden,M.E., and Rosenblatt,M., Proc.Roy.Soc.London, A361, (1978) 343.

11.) Rickerby,D.G., and Macmillan,N.H., J.Mater.Sci.,16 (1981) 1579.

12.) Evans,A.G., and Wilshaw,T.R., J.Mater.Sci., 12 (1977) 97

13.) Lawn,B.R., Hockey,B.J., and Wiederhorn,S.M., J.Mater. Sci., 15 (1980) 207.

14.) Frank,F.C., and Lawn,B.R., Proc.Roy.Soc.London, A299 (1967) 291.

15.) Hockey,B.J., Wiederhorn,S.M., and Johnson,H., "Fracture Mechanics of Ceramics", Vol.3, edited by R.C.Bradt, D.P.H.Hasselman, and F.F.Lange, (Plenum Press, New York 1978) 379.

16.) Wiederhorn,S.M., and Hockey,B.J., J.Mater.Sci., 18 (1983) 766

17.) Evans,A.G., "Treatise on Materials Science and Technology", Vol.16, edited by C.M.Preece, (Academic Press, New York) (1979) 1.

18.) Wiederhorn,S.M., and Lawn,B.R., J.Amer.Ceram.Soc., 62 (1979) 66.

19.) Roesler,F.C., Proc.Phys.Soc.London Sect., B69 (1956) 981.

20.) Gulden,M.E., J.Amer.Ceram.Soc.Communications, 64 (1981) C-59.

21.) Dimond,C.R., Kirk,J.N., and Briggs,J., Wear of Materials, ASME, New York (1983) 333.

22.) Kingon,A.I., Stone,N.A., and Carr,N.S., "High Tech. Ceramics", edited by P.Vincenzini, (Elsevier, Amsterdam, 1987) 2657.

23.) Kingery,W.D., "Introduction to Ceramics", John Wiley and Sons, Inc., (1960) 470.

24.) Routbort,J.L., Scattergood,R.O., and Turner,P.A.L., Wear, 59 (1980) 363.

25.) Ritter,J.E., Jakus,K., Viens,M., and Breder,K., Proc. 7th Int.Conf.on Erosion by Liquid and Solid Impact, Cambridge, (1987) 55-1.

26.) Hutchings,I.M., Wear, 35 (1975) 371.

27.) Brown,R., and Edington,J.W., Wear, 71, (1981) 113

28.) Yust,C.S., and Crouse,R.S., Wear, 51 (1978) 193.

29.) Recht,R.F., J.Appl.Math., (June 1964) 189.

30.) Lawn,B.R., Hockey,B.J., and Wiederhorn,S.M., J.Amer.Ceram.Soc., 63 (1980) 356.

31.) Giavanola,J.H., and Shockey,D.A., "Fracture Mechanics of Ceramics", Vol.6, edited by R.C.Bradt, A.G.Evans, D.P.H.Hasselman, and F.F.Lange, (Plenum Press, New York, 1983) 401.

32.) Lange,F.F., and Evans,A.G., J.Amer.Ceram.Soc., 62, No.1-2, (1979) 62.

33.) Pennefather,R.C., Hankey,S.E., Hutchings,R., and Ball,A., 3rd.Int.Conf.on the Science of Hard Materials, Nassau, Bahamas, 1987.

34.) Heathcock,C.J., Ball,A., and Protheroe, Wear, 74, (1981-82) 11.

35.) Ball,A., and Paterson,A.W., Proc.11th.Int.Plansee Semin. Reutte, 1985, Vol.2, Metallwerk Plansee, Reutte, (1985) 377.

36.) Miyoshi,K. Hattorii,S., Okada,T., and Buckley,D.H., NASA Technical Memorandum 88981, (1987).

37.) Heathcock,C.J., PhD. Thesis, University of Cape Town, (1980).

38.) Rayleigh,Lord, Phil.Mag., 34, (1917) 94.

39.) Preece,C.M., "Treatise on Materials Science and Technology" Vol.16., edited by C.M.Preece, (Academic Press, New York, 1979) 1.

40.) Vyas,B., and Preece,C.M., J.Applied Phys., 47, (1976) 5133.

41.) Hickling,R., and Plesset,M.S., Phys.Fluids, 7, (1964) 7.

42.) Hannson,I., Morch,K.A., and Preece,C.M., Ultrasonics Int., Ipc.Sci. and Tech. Press Ltd., Guildford. U.K. 77, (1978) 267.

43.) Hobbs,J.M., "Erosion by Cavitation or Impingement" ASTM.STP 408, (1967) 159.

44.) Rao,P.V., Seetharamai,K., and Rama Char,T.L., J.Electrochem.Soc.India, 23, (1974) 7.

45.) Stevens,R., "Zirconia and Zirconia Ceramics", Magnesia Elektron Ltd. (1986)

46.) Evans,A.G., and Charles,E.A., J. Amer.Ceram.Soc., Vol.59, 7, (1986) 371.

47.) Lammer,A., Mat.Sci and Technology, Vol.4, (1988), 949.

48.) Ruff,A.W., and Ives,L.K., Wear, 35, (1975) 195.

49.) Evans,P.A., Stevens,R., and Binner,J.G.P., Brit.Ceram. Trans.J., 83, (1984) 39.

50.) Ball,A., Wear, 91, (1983) 201.

51.) Rice,R.W., Ceramic Eng.and Sci.Proc., 6, No's 7-8, 940.

52.) Doyle,R.A, and Ball,A., EMSSA Proc., Durban, (1988).

53.) Hutchings,I.M., and Levy,A., Wear 131 (1989) 105.

54.) Nabarro,F.R.N., "Theory of Crystal Dislocations", Clarendon Press, Oxford, (1967).

55.) Hutchings,I.M., Winter,R.E., and Field,J.E., Proc.Roy. Soc.London, A348, (1976), 379.

56.) Tabor,D., "The Hardness of Metals", Clarendon Press, Oxford, (1951)

57.) Gupta,T.K., J.Mat.Sci., 9, (1974), 1585.

58.) Wada,S., and Watanabe,N., J.Ceram.Soc.Japan, 95, No.9, (1987) 5.

59.) McLachlan,D.S., Mater.Res.Bull., 8, (1973) 34.

60.) Srinivasan,S., and Scattergood,R.O., Wear, 128, (1988) 139.